Master's Degree Thesis

Inter-University Master's Degree in Nuclear Physics

Faculty of Physics, University of Seville

Modelling of a plasma break-down for the SMART tokamak

Author:

Daniel López Aires[1]

Supervisors:

Dr. Manuel García Muñoz[2]

Dr. Carlos Soria del Hoyo[3]

September 7, 2020

[1]E-mail addres: danlopair@gmail.com

[2]Department of Atomic, Molecular and Nuclear Physics, Faculty of Physics, University of Seville

[3]Department of Electronics and Electromagnetism, Faculty of Physics, University of Seville

Abstract

Achieving controlled nuclear fusion on Earth could be a decisive step on the quest towards green energy production since it would bring a virtually renewable energy source without CO_2 emissions. The Plasma Science and Fusion Technology group of the University of Seville is currently designing a magnetic fusion device, a *spherical tokamak* for controlled nuclear fusion research, called SMall Aspect Ratio Tokamak (SMART).

This thesis will model the first phase of the initiation of a tokamak (tokamak start-up), the break-down phase, in which the fuel will transition from the gas state to the plasma state, making use of the Fiesta toolbox. The fundamental of tokamak physics and tokamak start-up will also be reviewed. The current waveforms of the SMART coilset have been optimized to achieve the desired plasma equilibrium and allow the break-down of the pre-fill gas by reducing the stray poloidal magnetic field and maximizing the loop voltage induced by the inductor solenoid. Several criteria have also been applied to test the feasibility of the break-down phase, such as the Paschen's break-down curve, the estimation of the avalanche time, and the calculation of the connection length. The electric potential gained by the electrons as they follow the magnetic field lines has been computed to estimate where the gas will break-down. Break-down of the gas without the use of any auxiliary heating method has been achieved, lasting few milliseconds for gas pressures about 10^{-4}Torr.

Acknowledgements

I would like to thank J. Lister, who referred me to Izaskun Garrido, who gave me the main reference to understand the RZIp code. I would also like to thank Geoff Cunningham for his help and comments which help me focus on the right issues regarding break-down, and which also provide us with the Fiesta repository on git and a brief Fiesta documentation.

Special thanks to my tutors, this months of work have been really valuable, I have learned a lot, especially about team work in a multidisciplinary environment. I also have to apologize to Carlos for not telling him all the rapid upgrades the SMART reactor was suffering to ensure proper break-down conditions, isolating him a bit from the group and from my work. Thanks to Eli, for her help supervising this document.

Special thanks to Scott, who, despite arriving to the group in march, have learned very rapidly and have played a critical role in the changes in the SMART reactor, and to Alessio and Manu too, who also played a critical role in the changes from the engineering point of view.

I would also like to thank Jesús Poley, our talks about fusion and science in general were really interesting and helpful for both of us. Thanks to Antonio for his help with Inkscape. Special mention to the CS-GO team for all the good Friday nights during the Covid-19 quarantine.

Contents

Chapter 1

Introduction

1.1 Nuclear fusion as an energy source

Nowadays, the human kind is beginning to understand the damage its activity is causing on Earth, that could lead to the destruction of the planet we live in and, as a consequence, of ourselves. A radical change is needed in human's life before it is too late. One fundamental step is to stop using fossil fuels as an energy source, and use renewable sources instead, like wind energy, solar energy, or geothermal energy. However, there is another energy source, virtually unlimited that could provide a huge step forward this transition, *nuclear fusion*.

Nuclear fusion is a type of nuclear reaction in which two or more atomic nuclei (reactants) X and Y interact and produce a heavier nuclei, generally in an excited state $(X+Y)*$. This compound nuclei could de-excitate by emiting electromagnetic radiation and, if the excitation energy is sufficiently high, by releasing neutrons (evaporation).

$$X + Y \rightarrow (X+Y)* \tag{1.1}$$

Applying the conservation of energy to the reaction, using the laboratory reference frame

$$\begin{aligned} E_X + E_Y = E_{(X+Y)*} = E_{(X+Y)} + E_{\text{exc}} \Rightarrow T_i + (m_X + m_Y)c^2 = T_f + (m_X + m_Y)c^2 + E_{\text{exc}} \\ \Rightarrow T_f - T_i \equiv Q = -E_{\text{exc}}, \end{aligned} \tag{1.2}$$

Since the excitation energy E_{exc} is always positive, the Q factor of the reaction is negative, meaning that there is a reference frame in which $T_f = 0$, but T_i can never be zero. This means that this reaction is an endothermic reaction, it needs energy to take place.

The need of energy to produce a nuclear fusion reaction can be easily understood. Due to the positive charges of the nuclei, their Coulomb interaction is repulsive. However, not always the interaction is repulsive, if the nuclei are close enough, the nuclear interaction appears, and since its much more intense than the electromagnetic interaction, the dominant interaction is nuclear, which will attracts the nuclei, enabling them to approach enough so they can fuse into a new nuclei. If we plotted the potential between two nuclei, it would look similar to the one on figure 1.1.

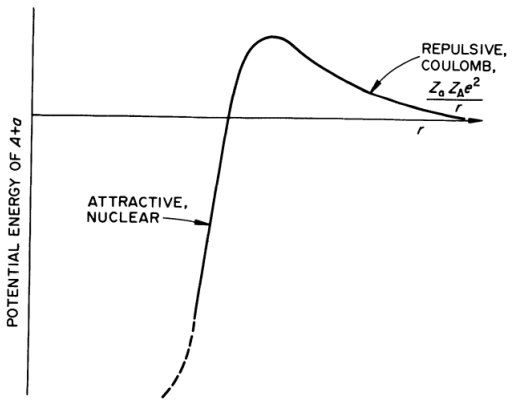

Figure 1.1. Coulomb barrier between two nuclei of mass number A and a. $e = e/(4\pi\varepsilon_0)$. Source: [1].

There are two regions, the region for $r >>$, in which the nuclei are far away from each other so there is no nuclear interaction between them and the potential is the Coulomb potential, and the $r <<$ region, in which the nuclear interaction appears, so the potential is the nuclear potential and the nuclei attract each other. The point where Coulomb interaction is compensated by the nuclear interaction is usually estimated as $R_N \simeq 1.45(A_1^{1/3} + A_2^{1/3})$fm, where A_1,A_2 are the mass number of the nuclei (A and a in figure 1.1).

The main challenge of nuclear fusion reactions is that the Coulomb barrier have to be overcomed, allowing the nuclei to approach enough so they can fuse into a new nuclei.

Although nuclear fusion reactions need energy to take place, the reactions could release more energy than the needed to stimulate it. This can be understood taking into account the concept of binding energy $B(N, Z)$, which is the energy needed to split a nuclei into its components,

$$B(A, Z) \equiv Zm_p + (A - Z)m_n - [M(A, Z) - Zm_e])c^2, \tag{1.3}$$

where $M(A, Z)$ is the mass of an atom of atomic number Z and mass number A, and m_p, m_n and m_e are the proton, neutron and electron masses respectively.

If B/A is plotted, figure 1.2 is obtained. B/A increases with A up to ^{56}Fe, and then it starts decreasing. This means that if combining elements to the left of ^{56}Fe, the compound nuclei is more stable than the initial nuclei, and the difference of binding energy from the stable compound nuclei and the less stable separate nuclei is released in the form of kinetic energy. Equivalently, if a nuclei heavier than ^{56}Fe splits into lighter nuclei, since the final nuclei will have higher binding energy than the original nuclei, the difference of binding energy will be released.

Figure 1.2 essentially explains why energy can be obtained from fission reactions, which have lead to the creation of nuclear power plants to obtain energy by fission reactions. But, in the same way it suggest that we could obtain energy as well by pursuing nuclear fusion reaction. In both cases, the fundamental condition to obtain energy is that the energy released is greater than the energy applied. In energy context, it is defined a variable called Q factor which is the ratio between the power obtained and the power applied to the system,

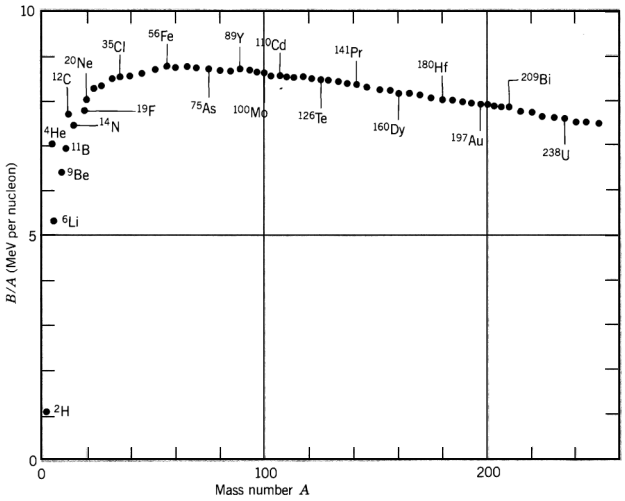

Figure 1.2. Binding energy per nucleon. The maximum B/A correspond to ^{56}Fe, the most stable element. Source: [2].

$$Q = \frac{P_{\text{obt}}}{P_{\text{app}}}. \tag{1.4}$$

How can we achieve nuclear fusion reactions on Earth so it can be used as an energy source (*controlled nuclear fusion*)? The first challenge is that for nuclear fusion to happen, the Coulomb barrier needs to be overcomed (actually, considering quantum tunneling, energy lower than the needed to surpass the Coulomb barrier would be needed to allow fusion reactions). Nuclear fusion reactions considered to be pursued on Earth involve Deuterium, ${}^{2}_{1}\text{H}$ because it is an abundant element, it exist on Earth's oceans comprising 0.015 atom percent of the hydrogen in sea water with the volume of about $1.35 \cdot 10^{9}$ km^{3} [3] (section 1.3). The possible reactions are:

1. ${}^{2}_{1}\text{H} + {}^{2}_{1}\text{H} \rightarrow {}^{3}_{1}\text{H}(1.01\text{MeV}) + p(3.03\text{MeV})$,
2. ${}^{2}_{1}\text{H} + {}^{2}_{1}\text{H} \rightarrow {}^{3}_{2}\text{He}(0.82\text{MeV}) + n(2.45\text{MeV})$,
3. ${}^{2}_{1}\text{H} + {}^{3}_{1}\text{H} \rightarrow {}^{4}_{2}\text{He}(3.52\text{MeV}) + n(14.06\text{MeV})$,
4. ${}^{2}_{1}\text{H} + {}^{3}_{2}\text{He} \rightarrow {}^{4}_{2}\text{He}(3.67\text{MeV}) + p(14.67\text{MeV})$,

where the kinetic energy each product carries is also indicated. Their cross-sections are plotted in figure 1.3, where the cross-section of the two ${}^{2}_{1}\text{H}$-${}^{2}_{1}\text{H}$ reactions have been added, and the X-axis is the projectile energy, ${}^{2}_{1}\text{H}$, assuming the target nuclei at rest. ${}^{2}_{1}\text{H} + {}^{3}_{1}\text{H}$ reaction is the best option since its cross-section is the highest, and it peaks at the lowest energy[1].

[1]Tritium, ${}^{3}_{1}\text{H}$, do not exist naturally on Earth's, but it could be produced by certain nuclear reactions with

For the most favourable reaction, a relative energy between the projectile and the target nuclei of about 100keV is needed. This energy would mean a temperature of about 10^8K ($E = K_B T$), hotter than the Sun's core temperature, which is estimated as 10^7K [2]. The Sun and all the stars emit energy due to nuclear fusion, although different nuclear reactions take place in the stars. In the case of the Sun, the reactions that take place are the *p-p* chain[3].

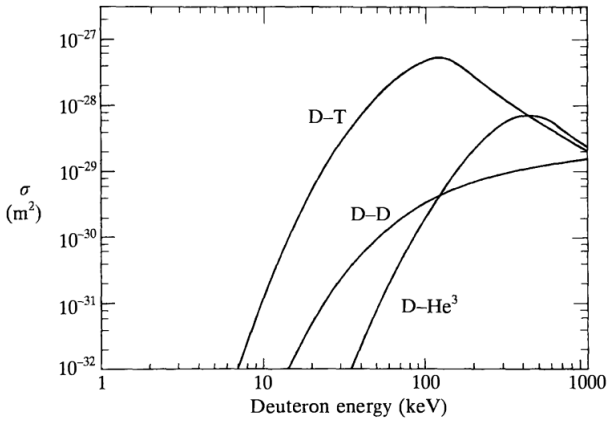

Figure 1.3. Cross-section of the fusion reaction involving Deuterium (D). The X-axis is the projectile energy, ${}^2_1$H, assuming the target nuclei at rest. The D-D cross-section is the sum of the cross-section of the two D-D fusion reactions. Source: [4]

At this extremely high temperatures, the fuel is in the plasma state. *A plasma is a quasineutral gas of charged and neutral particles which exhibits collective behavior* [5]. Stars confine the fuel via gravitational forces. How could the nuclear fuel be confined on Earth's at such temperatures? Since an object as massive as an star can not be made, and taken into account that there is no material that can withstand such high temperatures, other approaches are needed. Nowadays, there are mainly two methods:

- Inertial confinement. With the use of lasers a small region could be extremely heated and compressed so that a plasma can be formed. The National Ignition Facility (NIF)[4] is a USA's facility researching this way to obtain controlled nuclear fusion.

- Magnetic confinement. This the most advanced method to pursue nuclear fusion on Earth. It relies on the fact that nuclei are charged, so they could be confined in a closed space with the use of electromagnetic fields.

This thesis will be focused on magnetic confinement, in particular in a certain type of magnetic confinement devices, tokamaks.

The ${}^2_1\mathrm{H} - {}^3_1\mathrm{H}$ reaction produced an α particle (${}^4_2$He nuclei) carrying 3.52MeV and a neutron carrying 14.06MeV. The neutron, since it is neutral, leave the plasma without interaction but

Lithium, which is naturally abundant on Earth. Because both ${}^2_1$H and Lithium exist in abundance on Earth, usually nuclear fusion as an energy source is referred as a *virtually renewable* energy source, there would be enough fuel for thousands of years and without creating long-lived radioactive waste [4] (section 1.2).

[2] https://nssdc.gsfc.nasa.gov/planetary/factsheet/sunfact.html.

[3] A good review can be found in Wikipedia, https://en.wikipedia.org/wiki/Proton%E2%80%93proton_chain_reaction.

[4] https://wci.llnl.gov/facilities/nif.

the α particles are confined by the magnetic fields, and it can transfer its energy to the plasma by collision with the plasma particles. This is called *α-heating*. The power balance requires that the power applied to the plasma to heat it P_{app} plus the α-heating power P_α have to balance the loss power P_{l}, $P_{\text{app}} + P_\alpha = P_{\text{l}}$. The α-particles heating suggest a scenario in which there would not be neccesary to apply external heating could be achieved. This would mean $Q \to \infty$. This is called *ignition*, and it would be crutial for commercial nuclear fusion power plants. Up to date, this is a long term goal, but nowadays the JET tokamak have achieved $Q > 0$, i.e., has produced energy by nuclear fusion reactions, although the energy received was lower than the applied, and the under-construction ITER reactor[5] seeks to prove that $Q > 10$ is achievable, that is, that the enery produced can surpass the applied energy by a factor of 10 at least.

1.1.1 Definition of a plasma

The definition of a plasma of [5] has been previously said, *a plasma is a quasineutral gas of charged and neutral particles which exhibits collective behavior*. The definitions of collective behaviour and quasineutrality are as follow:

- *Quasineutrality*. A plasma is composed of neutral and charged particles, ions and electrons, such that the net charge is zero. A neutral plasma (in equilibrium) will have the same charged particle density, n_0. Assuming for both ions and electrons the same charge, e, if a point charge q is inserted in the plasma, the electrostatic potential is, if the coordinate system is centered at the test charge

$$\phi(r) = \frac{1}{4\pi\epsilon_0}\frac{q}{r}\exp\left[\frac{-r}{\lambda_{\text{Debye}}}\right] \equiv \phi_0(r)\exp\left[\frac{-r}{\lambda_{\text{Debye}}}\right], \tag{1.5}$$

  where $\phi_0(r)$ is the vacuum potential of the point charge, and $\lambda_{\text{Debye}} = \sqrt{\frac{\epsilon_0 k_B T_e}{e^2 n_0}}$ is the Debye length, with T_e the plasma temperature. This means that the potential is shielded if $r > \lambda_{Debye}$. Therefore, if the size of the plasma L is much greater than λ_{Debye}, any charge accumulation will be shielded, so that the plasma remains neutral. $L >> \lambda_{\text{Debye}}$ is the *quasineutrality condition*.

  However, the shielding of local charge accumulations could only be done if the plasma has enough particles surrounding the charge accumulation to shield it, and this leads to another condition, $N_D >> 1$, where $N_D = n_0\frac{4}{3}\pi\lambda^3_{Debye}$ is the number of particles in a sphere of radius λ_{Debye} surrounding the charge, called the "Debye sphere". This two conditions have to be satisfied to achieve quasineutrality.

[5] https://www.iter.org/.

- *Collective behaviour.* This means that the motion of the gas has to be governed mainly by electromagnetic forces rather than hydrodynamic forces, i.e., collisions between the particles. If ω is the frequency of typical plasma oscillations and τ is the mean time between collisions with neutral atoms, the condition for an ionized gas to behave like a plasma is $\omega\tau > 1$.

An ionized gas is considered a plasma if the three previous condition are satisfied (the two conditions of quasineutrality and the condition of collective behaviour).

1.2 Confinement of charged particles in electromagnetic fields

If a particle of charge q is set in a magnetic field $\vec{B}$, the field exerts a force upon the charged particle given by Lorentz's law:

$$\vec{F}_{\text{mag}} = q\vec{v} \wedge \vec{B}, \tag{1.6}$$

where $\vec{v}$ it the velocity of the particle. Note that the force is perpendicular to the velocity; if q moves an amount $d\vec{l} = \vec{v}dt$, the work done by the magnetic force is $dW = \vec{F}_{\text{mag}} \cdot d\vec{l} = q\vec{v} \wedge \vec{B} \cdot \vec{v}dt = 0$. The Lorentz force, hence, can not speed up the particle, but it can modify the trajectory of the particle.

To explore the motion of the particle, the simpler case is the case of a constant magnetic field $\vec{B}_0$. The equation of motion in an inertial frame is, by Newton's second law

$$m\frac{d\vec{v}}{dt} = \vec{F}_{\text{mag}} = q\vec{v} \wedge \vec{B}_0, \tag{1.7}$$

where m is the mass of the particle. If we assume $\vec{B}_0 = B_0 \hat{z}$, (1.7) leads to

$$\left.\begin{aligned} m\frac{dv_x}{dt} &= qB_0 v_y, \\ m\frac{dv_y}{dt} &= -qB_0 v_x, \\ m\frac{dv_z}{dt} &= 0, \end{aligned}\right\} \Rightarrow \left.\begin{aligned} \frac{d^2v_x}{dt^2} &= -\omega_c^2 v_x, \\ \frac{d^2v_y}{dt^2} &= -\omega_c^2 v_y, \\ m\frac{dv_z}{dt} &= 0, \end{aligned}\right\} \tag{1.8}$$

where $\omega_c \equiv qB_0/m$ is the *Larmor frequency.* The solution of (1.8) can be written as

$$\left.\begin{aligned} v_x(t) &= v_\perp \cos(\omega_c t), \\ v_y(t) &= v_\perp \sin(\omega_c t), \\ v_z(t) &= v_\parallel, \end{aligned}\right\} \Rightarrow \left.\begin{aligned} x(t) &= x(0) + R_{\text{L}} \sin(\omega_c t), \\ y(t) &= y(0) - R_{\text{L}} \cos(\omega_c t), \\ z(t) &= z(0) + v_\parallel t, \end{aligned}\right\} \tag{1.9}$$

where $v_\perp$ and $v_\parallel$ are the modules of the component of the velocity perpendicular and parallel to the magnetic field respectively, $(x(0), y(0), z(0))$ is the initial position of the particle and $R_{\text{L}} \equiv v_\perp/\omega_c$ is the *Larmor radius.*

The particle describes a circular motion of radius R_L in the plane perpendicular to the field, centered on $(x(0), y(0))$, and an uniform motion parallel to the field, due to its velocity along the magnetic field, that is, it follows an helical motion. The axis of this helix is called *guiding centre*. Figure 1.4 shows this motion.

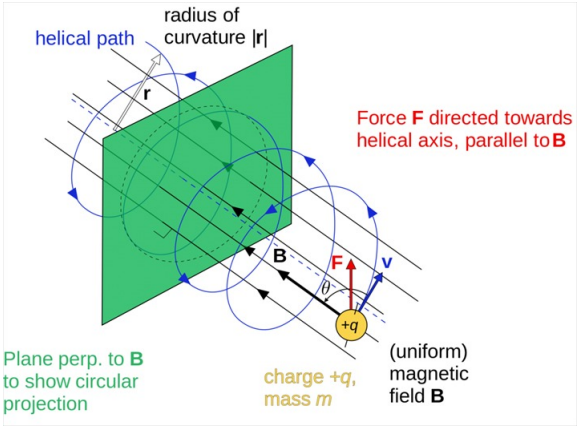

Figure 1.4. Motion of a charged particle in an uniform magnetic field. The particle follows an helical trajectory. Source: google images, 2019.

For more complex situations, like the presence of an electric field or non-uniform electromagnetic fields, one approach to understand the total motion of the particle is to treat separately the additional force that acts upon the particle, which results either on an acceleration parallel to the magnetic field or a drift of the guiding centre. The most common are going to be briefly mentioned:

- Acceleration due to $E_\parallel$

  A parallel (to the magnetic field) electric field $E_\parallel$ provides an acceleration given by

$$m\frac{dv_\parallel}{dt} = qE_\parallel \tag{1.10}$$

- Acceleration due to $(\nabla B)_\parallel$, magnetic mirror effect

  If the magnetic field has a gradient parallel to $\vec{B}$ (B is the magnitude of the magnetic field, so ∇B is a vector), and the particle has a velocity perpendicular to $\vec{B}$, there is a force parallel to the magnetic field, which can be used to confine the particle. It is easier to understand by considering energy conservation, and treating the charged particle as a magnetic dipole of magnetic moment $\mu = mv_\perp^2/2B$. The force upon the particles is then

$$\vec{F} = -\mu(\nabla B)_\parallel \frac{\vec{B}}{B} \tag{1.11}$$

  where $(\nabla B)_\parallel$ is the parallel component of (∇B).

  It can be shown [4] (section 2.7) that μ is an adiabatic invariant, which means it remains almost constant during the motion of the particle. Consider a non-uniform magnetic field displaying regions of low and high magnetic field intensity, like the one on figure 1.5,

called *magnetic bottle*. The conservation of the energy and the magnetic moment in two points i and f leads to

$$E_{\mathrm{i}} = E_{\mathrm{f}} \Rightarrow \frac{1}{2}m(v_{i\perp}^2 + v_{i\parallel}^2) = \frac{1}{2}m(v_{f\perp}^2 + v_{f\parallel}^2),$$
$$\mu_{\mathrm{i}} = \mu_{\mathrm{f}} \Rightarrow \frac{mv_{\mathrm{i}\perp}}{2B_{\mathrm{i}}} = \frac{mv_{\mathrm{f}\perp}}{2B_{\mathrm{f}}}. \tag{1.12}$$

If the field B increases from point i to f, $v_\perp$ has to increase too, which means that $v_\parallel$ has to decrease. This suggests that if the field is large enough, a point f with $v_{f\parallel} = 0$ can exist, and in this point the particle bounces (by the action of the force) and moves in the opposite direction.

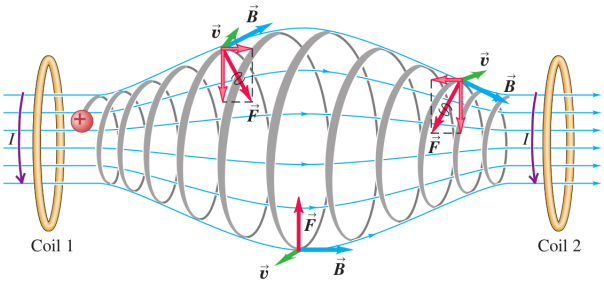

Figure 1.5. Magnetic bottle. The conservation of the energy and the magnetic moments enables the confinement of particles with this set up. Source: [6].

- $\vec{E} \wedge \vec{B}$ drift

  The drift velocity of the guiding centre $\vec{v_d}$ due to a force $\vec{F}$ is

  $$\vec{v}_d = \frac{1}{q}\frac{\vec{F} \wedge \vec{B}}{B^2}. \tag{1.13}$$

  With an electric field perpendicular to the magnetic field, the particle undergoes the so-called $\vec{E} \wedge \vec{B}$ drift, which can be easily computed by using (1.13) with $\vec{F} = q\vec{E}$, resulting in a motion independent on the charge. This motion is shown in figure 1.6 (a).

- ∇B drift

  If we have a ∇B perpendicular to $\vec{B}$, the Larmor radius will vary and as a result, the total motion of the particle will be an egg-shaped motion (see figure 1.6 (b)). The drift velocity is given by

  $$\vec{v}_{\nabla B} = \frac{mv_\perp^2}{2q}\frac{\vec{B} \wedge \nabla B}{B^3}. \tag{1.14}$$

- Curvature drift

If the guiding centre of a charged particle is following a curved field line, it undergoes a drift due to the centrifugal force. If the field lines have a constant radius of curvature R_c, the drift velocity is

$$\vec{v}_c = \frac{mv_\parallel^2}{qB^2}\frac{\vec{R}_c \wedge \vec{B}}{B^2}, \tag{1.15}$$

where $\vec{R}_c$ points from the center of the radius of curvature towards the outside (See figure 1.6 (c)).

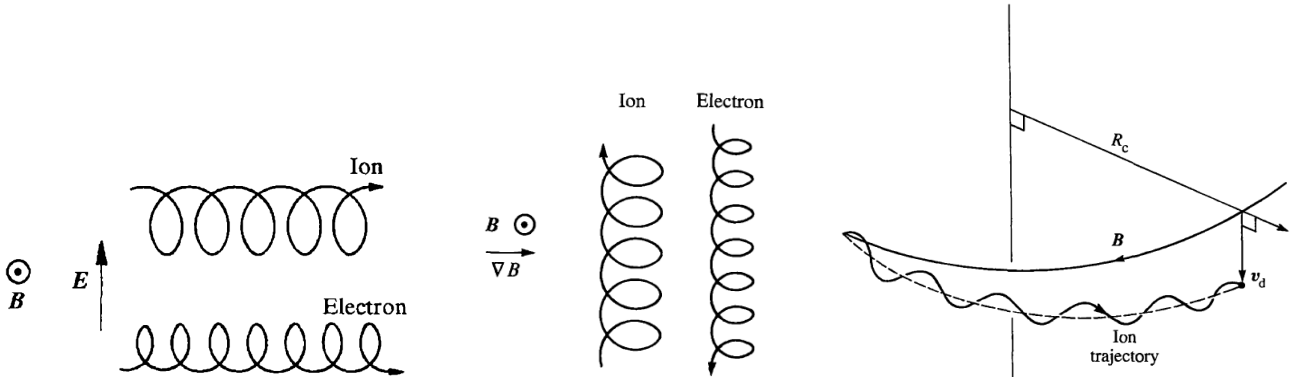

(a) $\vec{E} \wedge \vec{B}$ drift on an ion and an electron. The drift velocity points to the right, so both ions and electrons move to the right, since this drift do not depend on the charge, modifying the circular motion into an egg-shaped motion.

(b) ∇B drift on ion and electron. The drift velocity points upward or downward, depending on the charge.

(c) Curvature drift of an ion due to a curved magnetic field. It is shown the direction of the drift velocity.

Figure 1.6. $\vec{E} \wedge \vec{B}$, ∇B and curvature drifts. Source: [4].

1.3 Tokamaks

Many devices have been created to achieve nuclear fusion by magnetic confinement. The basis of one of the first devices, magnetic mirrors, have already been described. Here we are going to focus on toroidal devices, in particular in a certain type of devices called *tokamaks* [4, 3] (for a more divulgative yet formal and descriptive point of view, it is highly recommended to see the series of articles [7, 8, 9, 10]). Its name is a Russian acronym for toroidal chamber with an axial magnetic field. If a toroidal solenoid is considered, it is a closed geometry with a magnetic field that is null at its outside and it goes as $1/R$ at its inside, where R is the radial coordinate (see figure 2.1 (a)). However, this is not enough to confine particles inside the solenoid because of the drifts described previously. The non-uniformity of the magnetic field at its inside leads to

a ∇B drift, that drift the ions downward and the electrons upward, since (1.14) depends on the charge q. This charge separation will create an electric field perpendicular to the magnetic field, so the particles will experience a $\vec{E} \wedge \vec{B}$ drift, that would drift outward both ions and electrons, provided that this drift does not depend on the charge. These drifts are shown in figure 1.7 (a).

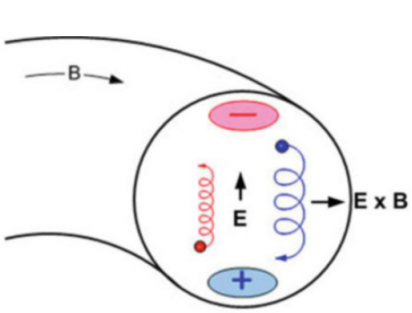

(a) Drifts in a torus. Source: [5].

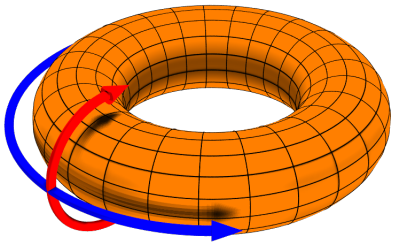

(b) Toroidal (blue) and poloidal (red) directions of a torus. Source: google images, 2019.

Figure 1.7. Drifts in a torus and definition of the poloidal and toroidal directions on a torus.

To overcome the drifts discussed above, *Tokamaks* confine the particles by twisting the magnetic field lines. For doing that, in addition to the toroidal field of the torus, a poloidal field is added (field in the poloidal direction, see figure 1.7 (b)). This poloidal magnetic field is created by the plasma itself.

Tokamaks need additional coils for controlling the plasma. The plasma itself tend to move radially outward due to poloidal field created by the plasma, which is greater in the inboard region than in the outward, and due to the toroidal shape of the plasma, the plasma pressure also creates an outward force. This outward force is called *hoop force* (see [11] for an illustrative explanation, and [3] for a rigurous treatment). This coils are called poloidal magnetic field coils (PF coils) since its role is to create poloidal field whose $\vec{J} \wedge \vec{B}$ force balance the hoop force. For doing that, the current flowing in this PF coils need to flow in the opposite direction to the plasma current. In addition, this coils also help create the elongated shape of tokamak plasmas. An additional set of coils called divertor coils are often used to created a *diverted* shape in the plasma, which will be explained later.

Figure 1.8 shows a sketch of a tokamak with its basics elements. The plasma is contained in the vacuum vessel (VV) (grey coloured in the figure). The toroidal field (green arrows) is created by the toroidal magnetic field coils, and the poloidal field is created mainly by the plasma itself,

and by the PF coils (plasma shaping). In the center of the device there is a transformer coil that induces a toroidal current in the plasma (red arrows) that creates the poloidal magnetic field. The resulting field lines are helical lines (yellow arrows), which confine most of the plasma particles. Since the plasma current is inductive, tokamaks operate in a pulsed regime. One the challenges of this device is the control of the plasma, and the electromagnetic instabilities that could arise in the plasma, which could lead to the loss of the plasma energy. This events are called *Disruptions*.

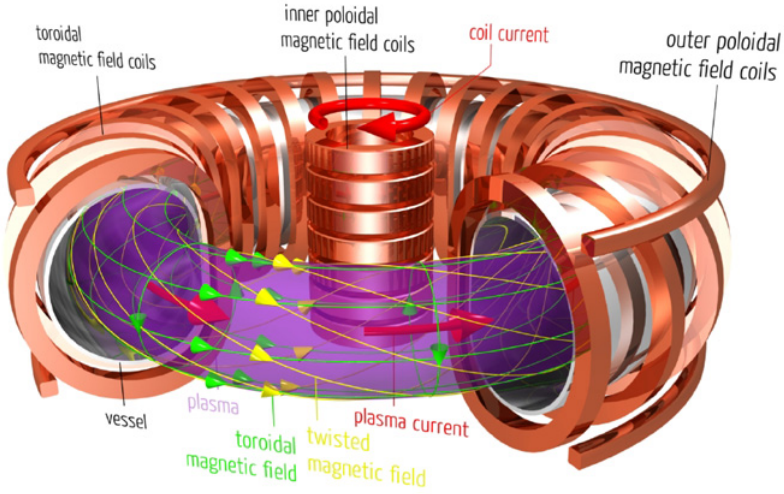

Figure 1.8. Sketch of a tokamak, showing its basic elements, the field lines and the plasma current. Source: google images, 2019.

For the initialization of a tokamak discharge, called *tokamak start-up*, the toroidal magnetic field must be previously stablished and the VV is filled with a gas. After the inductor coil induced the electric field by changing its current, the gas will be ionized creating a plasma (this is called *break-down*). This plasma will start to create the poloidal field that confines the particles. In the meantime, the plasma needs to be heated and the PF coils will be controlling its shape. There are several methods of heating the plasma; to begin with, the plasma current will heat the plasma due to Joule's effect, which is called ohmic heating. External methods of heating could be the use of electromagnetic waves (the electromagnetic waves will create oscillations of the plasma particles, increasing their energy), injection of neutral particles (the injected particles will accelerate the plasma particles by collisions with them, increasing their temperature), and many more (see chapter 5 of [4] for a description of heating methods[6]). Finally, the plasma will arrive at the desired configuration with the desired plasma current and shape, ending the start-up phase.

[6]The websites of currently operating tokamaks also provide information about the way they heat their plasmas.

1.4 Motivation: SMART, a SMall Aspect Ratio Tokamak for the University of Seville

The Plasma Physics and Fusion Technology Group of the University of Seville is designing a tokamak that will be operating the next year[7]. Its name will be SMall Aspect Ratio Tokamak (SMART), which reveal the main characteristic of the device, it will be a spherical tokamak rather than a standard tokamak. This reactor will not make fusion reactions; instead, as well as all the existing small and medium size reactors, it will focus on doing tokamak physics research such as plasma confinement, shape, instabilities, etc. This information will be used by large international facilities such as JET or ITER, which will make fusion reactions. The SMART missions are

- Study plasma transport and confinement in positive and negative triangularities.
- Develop novel diagnostic and control schemes.
- Examine electromagnetic stability and control of energetic particles.
- Train next generation of fusion physicists and engineers.

The main difference between a spherical tokamak and a tokamak is the aspect ratio of the device, which is the ratio of the major radius and the minor radius of the device. If the aspect ratio of the tokamak is < 2, the device is called *spherical tokamak*. Figure 1.9 shows a standard tokamak and a spherical tokamak.

Spherical tokamaks are a desirable approach to controlled nuclear fusion because they are more compact than regular tokamaks, which means lower costs, and spherical tokamak's plasmas displays better plasma properties such as the so called *safety factor* q and the β, which will be explained later (reviews of spherical tokamaks features vs regular tokamaks features can be found on [12, 13]).

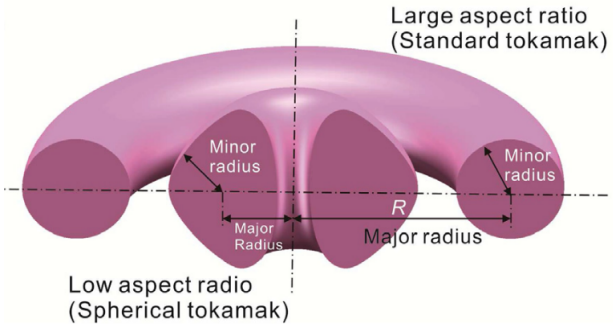

Figure 1.9. Tokamaks and spherical tokamaks. Source: [12].

Three operational phases have been designed for the SMART tokamak:

[7] http://www.psft.eu/.

- Phase 1. First plasma and proof-of-concept.
- Phase 2. Inclusion of Neutral Beam Injection (NBI) heating system. The goal of this phase is the demonstration of plasma shaping.
- Phase 3. This phase will explore fusion-relevant operations.

The main parameters of this three phases are shown in table 1.1. This parameters will be explained in the following sections. A 3D model of the SMART tokamak is shown on figure 1.10. The coilset configuration will be the same for the three phases.

(a) Reactor. (b) Coilset.

Figure 1.10. 3D plots of the SMART reactor. The coilset is symmetric with respect to the $Z = 0$ plane, and several coils are inside the vacuum vessel (VV). The ports in the VV are for plasma diagnosis and for plasma heating methods such as NBI and ECRH, which will be explained later. Source: [14].

1.5 Objectives and outline of the thesis

The goal of this work is to model the initial phase of the tokamak start-up, the break-down of the gas, of SMART, optimizing the device so that the gas breaks-down and turns into a plasma for the first operational phase and the first upgrade, phase two, without any additional heating method.

This thesis is organized as follows: chapter 2 presents the basics of tokamak physics, the simplest model of the plasma, and the fundamental equation to describe the tokamak equilibrium, the Grad-Shafranov equation, as well as the characterization of a tokamak plasma. Chapter 3 reviews the tokamak start-up, focusing on the break-down phase, introducing the

SMART				
		Phase 1	Phase 2	Phase 3
VV radius(m)		0.8		
VV height(m)		1.6		
Major plasma radius(m)		0.42		
Minor plasma radius(m)		0.24		
Plasma elongation κ		$\kappa < 2.1$		
Plasma triangularity δ		$-0.51 < \delta < 0.44$		
Plasma current(kA)		35	100	500
Toroidal field(T)		0.1	0.3	1.0
Flat-top time(ms)		20	100	500
External heating (KW)	ECRH	6 [2.4GHz]	6 [7.5GHz]	200 [- GHz]
	NBI	-	600	600

Table 1.1. Parameters of the phases of the SMART tokamak. Toroidal field is the toroidal field value at the plasma magnetic axis.

basic physics of this phase, as well as several criteria to ensure a proper break-down of the gas. Chapter 4 reviews the Fiesta toolbox used for computing the plasma equilibrium and the dynamic behaviour of the plasma using the RZIp model. Chapter 5 summarizes the simulation procedure followed in this work. Chapter 6 contains the simulation results, as well as the discussion of the results with other operating tokamaks. Finally, chapter 7 summarized the work carried out in this thesis, and discuss future work.

Chapter 2

Fundamentals of tokamak physics

In this chapter the fundamentals of tokamak physics will be reviewed. The first section includes the plasma model used in tokamak physics, the second section includes the derivation of the equation of the tokamak equilibrium configuration, and the third section reviews some basic tokamak parameters.

2.1 Magnetohydrodynamic model of a plasma

The Magnetohydrodynamic (MHD) model is a single fluid description of a plasma, i.e., it is a model that treats a plasma like a continuum matter, rather than as a set of particles. This is one of the simplest models to study a plasma, and it assumes several hypothesis, like quasineutrality or negligible electron inertia (see any book about plasma physics for further details, like [5]). The set of equations are

$$\frac{\partial \rho}{\partial t} + \nabla \cdot (\rho \vec{v}) = 0, \text{ [Mass conservation]} \tag{2.1}$$

$$\rho\Big[\frac{\partial \vec{v}}{\partial t} + (\vec{v} \cdot \nabla)\vec{v}\Big] = \vec{j} \wedge \vec{B} - \nabla p, \text{ [Momentum conservation]} \tag{2.2}$$

$$\vec{E} + \vec{v} \wedge \vec{B} = \eta \vec{j}, \text{ [Ohm's law]} \tag{2.3}$$

$$\frac{\partial}{\partial t}(p\rho^{-\gamma}) + (\vec{v} \cdot \nabla)(p\rho^{-\gamma}) = 0, \text{ [Adiabatic behaviour]} \tag{2.4}$$

$$\nabla \wedge \vec{E} = -\frac{\partial \vec{B}}{\partial t}, \tag{2.5}$$

$$\nabla \wedge \vec{B} = \mu_0 \vec{j}, \tag{2.6}$$

$$\nabla \cdot \vec{B} = 0, \tag{2.7}$$

where ρ is the plasma density, $\vec{v}$ its velocity, η its resistivity, p its pressure (in general the pressure is a tensor, but for this simplified model, it is considered an scalar magnitude), $\vec{j}$

its current density, γ is the adiabatic index, and $\vec{E}$ and $\vec{B}$ the electric and magnetic field the generated by the plasma. Note that the last three equations are a quasi-static limit of Maxwell's equations.

2.2 Grad-Shafranov equation

Figure 2.1(a) displays the coordinate system of toroidal devices. In an equilibrium situation, the magnetic field of a Tokamak produces an infinite set of nested toroidal magnetic flux surfaces[1] as shown in figure 2.2, and the magnetic field lines follow an helical path on them as they wind round the torus. The poloidal flux Ψ and the toroidal flux Φ between two magnetic surfaces are defined by

$$d\Psi \equiv \vec{B} \cdot d\vec{S}_\theta, \quad d\Phi \equiv \vec{B} \cdot d\vec{S}_\phi, \tag{2.8}$$

where dS_θ, dS_ϕ are the poloidal and toroidal surface elements, whose magnitude are defined in figure 2.1(b) (its unitary vector is perpendicular to the surface, and the sign is arbitrary, as usually in the magnetic fluxes), and $\vec{B}$ is the magnetic field. The basic condition for the

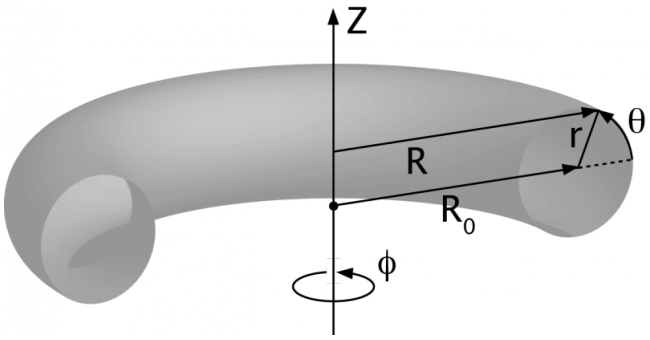

(a) Cylindrical coordinate system used in devices with torodial symmetry, (R, ϕ, Z). R_0 is called the major radius of the torus, r is called the minor radius. The circumference $R = R_0$ defines the toroidal or magnetic axis. Source: http://fusionwiki.ciemat.es/wiki/Toroidal_coordinates.

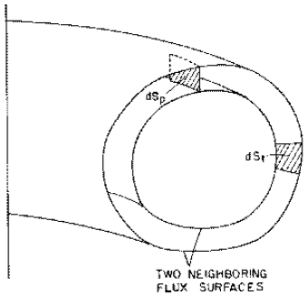

(b) Toroidal (T) and poloidal (P) surface elements between two magnetic flux surfaces. Source: [15].

Figure 2.1. Cylindrical coordinate system for toroidal devices, and definition of the poloidal flux in a torus.

equilibrium is that the force on the plasma be zero at all points, so the momentum conservation

[1] A given surface is a magnetic flux surface if it satisfies $\vec{B} \cdot \vec{n} = 0$, where $\vec{n}$ is the normal vector of the surface. That is, the magnetic field do not cross the surface. This is only a visual way to understand the magnetic field, since there would be an infinite number of magnetic flux surfaces inside a tokamak.

equation (2.2) leads to

$$\vec{j} \wedge \vec{B} = \nabla p. \tag{2.9}$$

This implies $\vec{B} \cdot \nabla p = 0$, so there is no presure gradient along the magnetic field lines, which means the magnetic surfaces are also pressure surfaces. (2.9) also implies $\vec{j} \cdot \nabla p = 0$, and as a consequence the current lie in the magnetic surfaces.

In what follows the Grad-Shafranov equation, one of the most fundamental equations of MHD equilibrium, will be derived. The idea for this equations is to rewrite (2.9) to have a scalar equation instead of a vector equation. From (2.7), taking into account the axysymmetry, and using the coordinate system of figure 2.1(a), setting $R_0 \equiv 0$,

$$\frac{1}{R}\frac{\partial (R B_{\mathrm{R}})}{\partial R} + \frac{\partial B_{\mathrm{Z}}}{\partial Z} = 0. \tag{2.10}$$

The function of that scalar equation will be the function ψ, called the *stream function*, which is defined as $\psi \equiv R A_\phi$, where A_ϕ is the toroidal component of the vector potential $\vec{A}$. With this function, the poloidal magnetic field can be written as

$$\left.\begin{aligned} B_{\mathrm{R}} &= \frac{-1}{R}\frac{\partial \psi}{\partial Z}, \\ B_{\mathrm{Z}} &= \frac{1}{R}\frac{\partial \psi}{\partial R}, \end{aligned}\right\} \Leftrightarrow \vec{B}_\theta = \frac{1}{R}\nabla\psi \wedge \hat{\phi}, \tag{2.11}$$

where $\hat{\phi}$ is the toroidal unit vector (the magnetic field can be expressed as $\vec{B} = \vec{B}_\theta + \vec{B}_\phi$). It can be shown that $\Psi = 2\pi\psi$ [15] (section 6.2). It is usual to label the magnetic surfaces with ψ, also called the magnetic flux. This means that $p = p(\psi)$, since magnetic surfaces are also pressure surfaces. From the symmetry of $\vec{j}$, it can be introduced a function f that verifies

$$\left.\begin{aligned} j_{\mathrm{R}} &= -\frac{1}{R}\frac{\partial f}{\partial Z}, \\ j_{\mathrm{Z}} &= \frac{1}{R}\frac{\partial f}{\partial R}, \end{aligned}\right\} \Leftrightarrow \vec{j_\theta} = \frac{1}{R}\nabla f \wedge \hat{\phi}\,. \tag{2.12}$$

Comparing (2.12) with (2.6) leads to

$$f = \frac{R B_\phi}{\mu_0}, \tag{2.13}$$

where μ_0 is the vacuum magnetic permeability and the subscript ϕ indicates the toroidal component. It can be shown that f is a function of ψ [4] (section 2.3). Equation (2.9) can be expanded as

$$\vec{j_\theta} \wedge \hat{\phi}\, B_\phi + j_\phi\, \hat{\phi} \wedge \vec{B}_\theta = \nabla p, \tag{2.14}$$

where j_ϕ, $\vec{j}_\theta$ are the magnitude of the toroidal current, and the poloidal current density vector respectively. Substituting (2.12) and (2.11) into (2.14), we get, using that $\hat{\phi}\cdot\nabla\psi = \hat{\phi}\cdot\nabla p = 0$ (consequence of the toroidal symmetry)

$$\frac{B_\phi}{R}\nabla f + \frac{j_\phi}{R}\nabla\psi = \nabla p. \tag{2.15}$$

Now, applying the chain rule on ∇f and ∇p,

$$\left.\begin{aligned}\nabla f &= \frac{df}{d\psi}\nabla\psi,\\ \nabla p &= \frac{dp}{d\psi}\nabla\psi,\end{aligned}\right\} \tag{2.16}$$

Introducing (2.13) and (2.16) into (2.15) lead to:

$$-\frac{\mu_0 f}{R^2}\frac{df}{d\psi}\nabla\psi + \frac{j_\phi}{R}\nabla\psi = \frac{dp}{d\psi}\nabla\psi \Rightarrow j_\phi = \frac{\mu_0 f}{R}\frac{df}{d\psi} + R\frac{dp}{d\psi}. \tag{2.17}$$

$\nabla\psi$ can be removed from (2.17) since $\nabla\psi = 0$ correspond to the trivial solution. To get j_ϕ as a function of ψ, we substitute (2.11) on (2.6), obtaining

$$\mu_0\vec{j} = \mu_0 j_\phi\,\hat{\phi} + \frac{1}{R}\nabla(RB_\phi)\wedge\hat{\phi} \Rightarrow -\mu_0 R j_\phi = R\frac{\partial}{\partial R}\Big(\frac{1}{R}\frac{\partial\psi}{\partial R}\Big) + \frac{\partial^2\psi}{\partial Z^2}, \tag{2.18}$$

Finally, if we substitute (2.18) on (2.17), we get the Grad-Shafranov equation,

$$R\frac{\partial}{\partial R}\Big(\frac{1}{R}\frac{\partial\psi}{\partial R}\Big) + \frac{\partial^2\psi}{\partial Z^2} = -\mu_0 R^2\frac{dp(\psi)}{d\psi} - \mu_0^2 f(\psi)\frac{df(\psi)}{d\psi}. \tag{2.19}$$

(2.19) is one of the fundamental equations of MHD equilibrium. It is a second order partial differential equation that calculates the equilibrium in toroidal devices, given the functions $p(\psi)$ and $f(\psi)$. In figure 2.2 (b), we can see a typical solution of this equation, showing that the surfaces are shifted with respect to the magnetic axis, which is the major radius of the innermost surface.

2.3 Tokamaks parameters

The most important parameters of a tokamak equilibrium, as well as about plasma shape and control will be introduced in this section.

2.3.1 Plasma shape and control in tokamaks

The first concept that must be introduced is the plasma boundary. The boundary of the plasma is the outermost closed magnetic surface contained in the VV, called *Last Closed magnetic Flux*

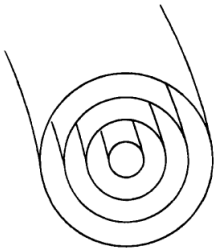

(a) Magnetic flux surfaces of a tokamak equilibrium, forming a set of nested cylindrical surfaces. Source: [4].

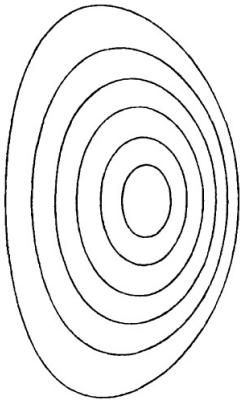

(b) Typical solution of the Grad-Shafranov equation. Source: [4].

Figure 2.2. Magnetic flux surfaces of a tokamak equilibrium, and typical solution of the Grad-Shafranov equation.

Surface, LCFS. The particles inside this outermost surface follow the field lines that remain in the plasma, but particles that follow the external field lines will end up escaping from the plasma and colliding with the VV (the particles follow the magnetic field lines, but if the magnetic field lines are not closed inside the VV, particles will collide with the VV as they follow them). The boundary can be created by a set of coils or by a limiting material that will touch the plasma (either the vacuum vessel or another element). The first method is to create the LCFS displaying one or more *X-points* by using a set of coils. X-points are saddle points where $\frac{\partial \psi}{\partial Z} = \frac{\partial \psi}{\partial R} = 0$, so the poloidal magnetic field is zero (see (2.11)). The outermost closed surface is called *separatrix*, and a plasma confined this way is called a *diverted plasma*, and the coils used to create it are called *divertor coils*. The second method is to limit the plasma by the VV or an specific material, so that the plasma is touching that material. The plasma is then called a *limited plasma*. In figure 2.3 (a) a limited plasma and a diverted plasma with one X-point is showed.

For shape control of the plasma, the following parameters are introduced to describe the

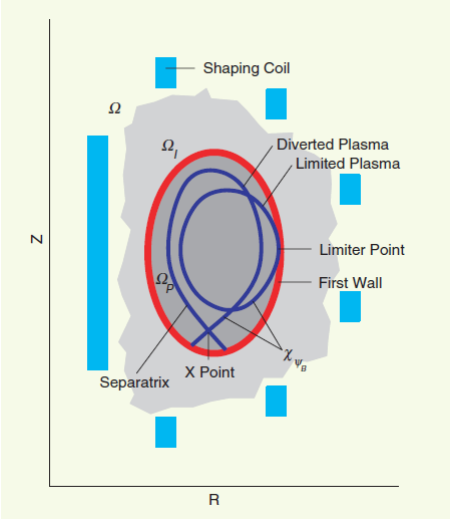

(a) Cross-section of a tokamak, showing its coils, and the boundaries (in dark blue) of a diverted plasma with one X-point and a limited plasma. Source: [8].

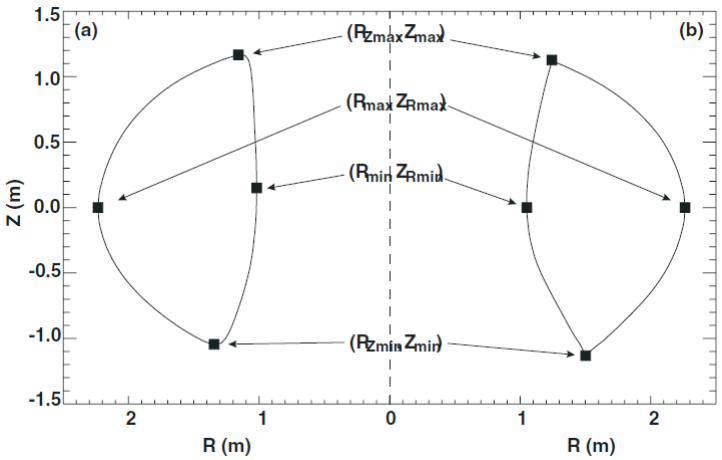

(b) Contour of the last close surface of a limited plasma (left) and a diverted plasma (right), showing the points used to describe the plasma shape. Source: [16].

Figure 2.3. Plasma geometry and plasma boundaries in tokamaks.

shape of the separatrix, with the points defined in figure 2.3 (b) [16]:

$$\begin{aligned}
\text{Major radius} \quad & R_{\text{geo}} \equiv (R_{\max} + R_{\min})/2, \\
\text{Minor radius} \quad & a \equiv (R_{\max} - R_{\min})/2, \\
\text{Aspect ratio} \quad & A \equiv R_{\text{geo}}/a, \\
\text{Elongation} \quad & \kappa \equiv (Z_{\max} - Z_{\min})/(2a), \\
\text{Upper triangularity} \quad & \delta_{\text{u}} \equiv (R_{\text{geo}} - R_{z_{\max}})/a, \\
\text{Lower triangularity} \quad & \delta_{\text{l}} \equiv (R_{\text{geo}} - R_{z_{\min}})/a.
\end{aligned} \tag{2.20}$$

2.3.2 Safety factor and normalized pressure

The confinement efficiency of the plasma in a tokamak is represented by β, which is the ratio between the volume averaged plasma pressure p and the energy density stored in the magnetic field or magnetic pressure, also called *normalized pressure*,

$$\beta \equiv \frac{p}{\frac{B^2}{2\mu_0}}. \tag{2.21}$$

Note it is a dimension-less magnitude. β defines the confinement efficiency because given a plasma with a certain average pressure, it determines the magnetic field necessary to confine it.

As a consequence, a high value of β is attempted. This also leads to the definition of poloidal β, β_θ,

$$\beta_\theta \equiv \frac{\int_{S_\theta} p dS_\theta / \int_{S_\theta} dS_\theta}{B_{\mathrm{a}}^2/2\mu_0}, \tag{2.22}$$

where $B_{\mathrm{a}} \equiv \mu_0 I/l$, I is the plasma current, S_θ is the poloidal cross-section of the plasma, and l its perimeter. The toroidal beta β_φ is defined in a similar way. It is also define the so-called *normalized beta* β_{N}, which is also a dimension-less magnitude, as

$$\beta_{\mathrm{N}} \equiv \frac{\beta_\varphi B_{\mathrm{T}} a}{I_{\mathrm{p}}\mu_0}, \tag{2.23}$$

where B_{T} is the toroidal field at the plasma magnetic axis and I_{p} the plasma current. One of the advantages of spherical tokamaks relative to standard tokamaks is that spherical tokamaks achieve higher β, which mean higher confinement efficiency [12].

Another relevant parameter is the *safety factor* q, which determines the stability of the plasma, higher values of q leads to greater stability. Each magnetic flux surface has its value, and its value is related to the helical paths of the field lines. If at a certain toroidal angle ϕ the field line has a certain position in the poloidal plane, and it returns to the same position in the poloidal plane after a change of the toroidal angle $\Delta\phi$, the q factor is

$$q \equiv \frac{\Delta\phi}{2\pi}. \tag{2.24}$$

As a consequence of this definition, higher values of q leads to more twisted helical magnetic field lines, which result in better confinement. $q = 1$ means that the magnetic field line returns to its initial position after one rotation around the torus. If $q = \frac{m}{n}$, where m and n are integers, it means that the field line returns to its initial position after m toroidal rotations and n poloidal rotations round the torus. The differential expression of the safety factor is

$$q \equiv \frac{d\Phi}{d\Psi}. \tag{2.25}$$

Making use of the parameters defined above, the fusion or thermonuclear power can be written as [17]

$$P_{\mathrm{fus}} \propto \beta_{\mathrm{N}}^2 \kappa (1+\kappa)^2 \frac{R_{\mathrm{geo}}^3 B_{\varphi_{\max}}^4}{q(a)^2} \frac{f(A)^2}{(A+1)^4 A^2}, \tag{2.26}$$

where $B_{\varphi_{\max}}$ is the maximum toroidal magnetic field, $f(A) \equiv 1.22A - 0.68$, and $q(a)$ is the safety factor at the plasma boundary. From this formula, increasing κ leads to greater fusion powers, which is another advantage of spherical tokamaks, their plasmas are more elongated than standard tokamaks plasmas.

Chapter 3

Tokamak start-up

The words *Tokamak start-up* refer to the processes that take place from the induction of the toroidal electric field by the inductor coil to the achievement of the target equilibrium configuration of the plasma, with the desired current and shape[1]. This processes can be divided into three phases:

1. Plasma break-down
2. Plasma burn-through
3. Plasma current ramp-up

This thesis is focused on the first phase, the break-down of the gas that is pre-filled into the vacuum vessel (VV). A review of all the phases will be given here. A plot displaying the variation of several variables during the start-up is showed on figure 3.1, which will be explained as the phases of the start-up are reviewed.

As previous conditions, the VV is pre-filled with a gas, and the toroidal field coils are turned on creating the toroidal magnetic field. In the first phase (blue coloured on figure 3.1), the toroidal electric field induced by the inductor coil accelerates the free electrons in the VV, and if they acquire enough energy, they could ionize the neutral atoms in the gas when colliding with them. The extracted electrons will also be accelerated, creating an avalanche of free electrons, called *Townsend avalanche*. As a result of this avalanche, the ionized gas start to develop a current, as can be seen on figure 3.1. The electron temperature T_e starts to increase

[1] A general review of the tokamak start-up can be found on [18]. As stated in the cited document, tokamak start-up receives attention only when there is a failure on it, so there is no extensive theory about it. However, to have commercial nuclear fusion power plants based on tokamaks this needs to change. A theoretical approach to the tokamak start-up problem can be found on the recent paper [19].

as well. When Coulomb collisions (collisions between charged particles) dominate along neutral atom-electron collisions, the break-down phase ends ant the burn-through phase begins.

In the *burn-through* phase, the plasma will ionize itself completely. In this phase, radiation losses starts to be relevant. This losses are caused by several factors such as Breemstrahlung radiation due to the deceleration of the electron in the collision with another atom, line-radiation of neutral atoms (neutrals) due to the excitation of the electronic shell of the neutrals followed by a de-excitation by emitting electromagnetic radiation, recombination of ions and electrons, and radiation from impurities from the non-perfect vacuum of the VV or impurities sputtered from the wall by the collisions of electrons with the VV (An extensive review of the power losses mechanisms and the burn-through phase can be found on [21], and a simpler approach can be found on [22]). Power losses starts to increase rapidly until a maximum is reached in the line radiation, as can be seen on fig 3.1[2].

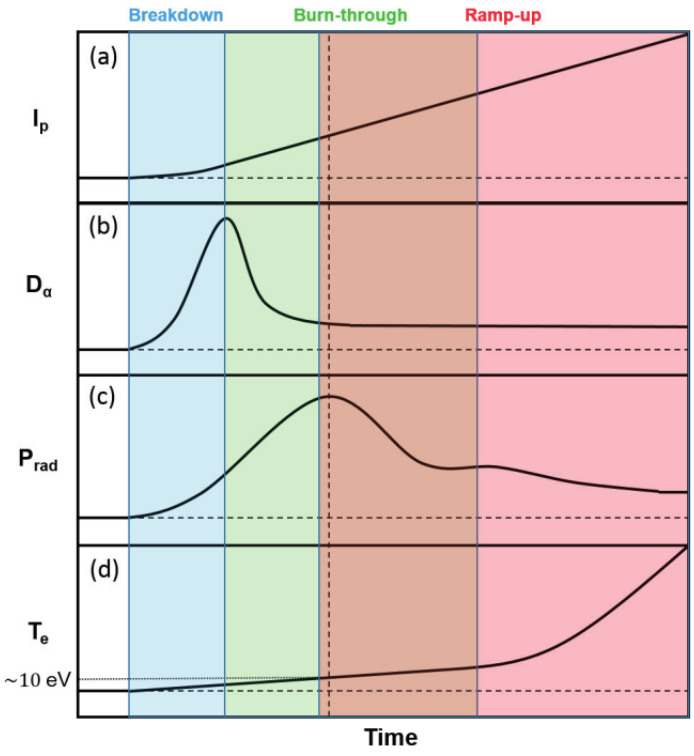

Figure 3.1. Time evolution of the plasma current (a), the line radiation of Deuterium (b), line-radiation losses (α line of Deuterium) (c) and electron temperature (d) during a tokamak start-up. Source: [20]. Deuterium is used as a prefilled gas here, since its line-radiation is showed. This plot assumes the beginning of the burn-through phase to be when the maximum of line radiation occurs.

This maximum can be easily understood. The line-radiation emissions should be proportional to the neutral atoms, since they are the ones whose electrons can be excited in collisions, decaying emitting electromagnetic radiation. Furthermore, it should be proportional to the electron density, since increasing the electron density means that more electrons could collide with neutral atoms, ionizing them. Provided that as the ionization proceed the electron density

[2]Note that the end of the avalanche phase and the beginning of the burn-through phase differs along the bibliography. For example, the source of fig 3.1, [20] defines the beginning of burn-through phase when the maximum in the line radiation is reached, while other articles suggest the beginning on the burn-through at an earlier stage, such as [19]. The approach of [19] will be followed in this thesis.

increases while the neutral density decreases, there must be a maximum point of line-radiation emissions.

In the meantime, at some point over this two phases, the poloidal field created by the plasma will start to be relevant, confining most of the particles. Once the plasma is completely ionized, the final phase, the *ramp-up phase* begins. In this phase the plasma current is increased by plasma heating, increasing the electron temperature (previously the increase in plasma current was mainly due to the increase of the electron density). Electromagnetic instabilities have to be avoided, since they could lead to an abrupt decrease of the plasma current.

3.1 Plasma break-down

The plasma break-down phase [23, 24, 25, 19] is the first phase on the tokamak start-up, and in this phase the pre-fill gas is ionized or *broken-down* into a plasma.

Plasma break-down is modelled using a *Townsend model*. In this model, the ions are considered at rest due to its enormous mass relative to the electron mass. When you apply an electric field in the toroidal direction E_φ to the gas in the VV, the electrons that are free in the tokamaks (there are always some) will be accelerated by the electric field, so if they acquire a determine amount of energy before a collision with a neutral atom, the neutral atom can be ionized. In the case of H_2, the energy to ionize it is about 15eV [19], leaving 2 electrons, which will be accelerated, and could produce more electrons, creating an electron avalanche called *Townsend avalanche*. However, not all the electrons are ionizing constantly, they end up colliding with the wall of the tokamak due to looses. The ionization and looses rate will be explored.

- Ionization rate ν_{ion}. If an electron produces α electrons per meter in the direction of the electric field, and there are N electrons, when traveling an infinitesimal distance dx, those N elecrons will produce an infinitesimal increase in the number of electrons $dN = \alpha N dx$. Dividing by the volume of the tokamak, we get the increase in the electron density, $dn_e = \alpha n_e dx$.

  The electrons are accelerated by the electric field, but due to of the collision with the neutral atoms that slow them down, they end up achieving a constant speed along the electric field direction $v_\parallel$. In that case, the differential distance traveled in a differential time dt is $dx = v_\parallel dt$, so the rate of creation of electrons or ionization rate ν_{ion} is

$$dn_e = \alpha n_e v_\parallel dt \Rightarrow \frac{dn_e}{dt} = \alpha n_e v_\parallel \equiv n_e \nu_{\text{ion}}, \tag{3.1}$$

where $\nu_{\text{ion}} \equiv \alpha v_{\parallel}$. α is called the *first Townsend coefficient*, which can be expressed as [21] (section 2)

$$\alpha = C_1 p \exp\Big(-\frac{C_2 p}{E_\varphi}\Big), \tag{3.2}$$

where p is the pre-fill gas pressure, E_φ is the toroidal electric field induced, and C_1, C_2 are experimentally determined constants (they are not absolute constants, they are constant for a certain range of E_φ/p, but for our case, they have a single value).

The constant parallel speed is proportional to E and p:

$$v_{\parallel} \propto \frac{E_\varphi}{p} \Rightarrow v_{\parallel} = C_3 \frac{E_\varphi}{p}. \tag{3.3}$$

C_3 is taken as 43 in [23]. However, for large $\frac{E_\varphi}{p}$ values, the previous formula is not valid, the electrons do not achieve a terminal velocity, which also means they do not create new electrons since they do not collide enough with the neutral atoms. This electrons are called *runaway electrons* [23, 19]. [23] proposed that they appear when $\frac{E_\varphi}{p} > 2 \cdot 10^4 \text{V m}^{-1}\text{Torr}^{-1}$. Torr is a pressure unit widely used in this context; 1Torr $\equiv 1/760\text{atm} = 101325/760\text{Pa} \simeq 133.32\text{Pa}$. As a consequence, the production of runaway electrons have to be avoided.

- Loss rate ν_{loss}. There are several sources of electron looses. The first source is due to the magnetic drifts discusses on section 1.3. Another source is the *stray* poloidal field B_θ present in the VV due to several factors, such as eddy currents in the VV, the inductor coil itself, which created poloidal field (border effects) or any magnetic material surrounding the VV. Due to this stray field, most of the magnetic field lines end up colliding with the VV, so electrons following them will eventually collide with the vessel. The dominant source is the stray field. If the length of the line parallel to the electric field is L, called the *connection length*, the loss rate due to the stray field can be expressed as

$$\nu_{\text{loss}} = \frac{v_{\parallel}}{L}. \tag{3.4}$$

Since the length of the magnetic field lines in a tokamak is mostly in the parallel direction (the toroidal direction) usually the total connection length (considering both poloidal and toroidal lengths) is taken as the parallel connection length. To decrease the effect of the stray field, it is common in tokamaks to create with the PF coils a region where the poloidal field is as low as possible, called *poloidal field null region*, so that there the field lines goes in the toroidal direction mostly, and electrons following them will collide

with each other. The connection length can be calculated numerically by integrating the magnetic field lines equation, but also an empirical formula is used to estimate it in the poloidal field null region [25]:

$$L \simeq 0.25 a_{\text{eff}} \frac{B_\varphi(R_{\text{null}})}{< B_\theta >}, \tag{3.5}$$

where $B_\varphi(R_{\text{null}})$ is the toroidal magnetic field at the center of this region R_{null} and $< B_\theta >$ is the average poloidal field in the surface of this region. Regarding a_{eff}, there are two visions in the bibliography:

i) a_{eff} is the linear distance to the closest wall. Sometimes this is estimated as the minor radius of the plasma target equilibrium configuration [21, 23].

ii) a_{eff} is the minor radius of the field null region [20, 25, 19].

The variation in the electron density considering both ionization and losses is

$$\frac{dn_e}{dt} = n_e(\nu_{\text{ion}} - \nu_{\text{loss}}). \tag{3.6}$$

The ionization rate can be assumed constant since electrons will acquire a constant speed quickly after the start of the ionization process. About the loss rate, the connection length may vary since as the toroidal electric field is induced inside the VV, eddy currents are also induced in the VV, which will affect the field, and hence alter the connection length L. However, as a first approximation, we could assume L to be constant. In that case the electron density as a function of time will be

$$n_e(t) = n_e(0) \exp\left[(\nu_{\text{ion}} - \nu_{\text{loss}})t\right], \tag{3.7}$$

where $n_e(0)$ is the electron density at $t = 0$, the time at which the toroidal electric field is induced. For a proper ionization of the gas, the ionization rate must be greater than the loss rate, so that the electron density increases. Imposing this, and introducing (3.1) and (3.4) in (3.6) gives

$$\frac{dn_e}{dt} = n_e v_\parallel(\alpha - 1/L) > 0 \Rightarrow (\alpha - 1/L) > 0 \Rightarrow \alpha L > 1, \tag{3.8}$$

taking into account $v_\parallel$ is the module of the speed, ergo, positive. For Townsend avalanche to proceed, $\alpha L > 1$ is needed. Setting $\alpha L = 1$ will give the limit condition so that the avalanche nor increase nor decrease. Introducing this condition on (3.2) gives

$$E_{\varphi_{min}} = \frac{C_2 p}{\ln(C_1 p L)}, \tag{3.9}$$

where $E_{\varphi_{min}}$ is the electric field needed for this condition. Since this condition do not ensures avalanche, [25] states that $E_\varphi > 2E_{\varphi_{min}}$ for a reliable start-up, so that the avalanche increases.

The plot of $E_{\varphi_{min}}$ as a function of p for a given L is called the Paschen's curve. An example is shown on figure 3.2, for H_2 as pre-fill gas. The constant are $C_1 = 510\text{m}^{-1}\text{Torr}^{-1}$ and $C_2 = 1.25 \cdot 10^4\text{Vm}^{-1}\text{Torr}^{-1}$. It can be seen from the figure that all the lines displays a minimum electric field needed for a certain pressure. This can be easily understood: for high pressures, the mean free-path will be too short (the mean free path λ is given by $\lambda = 1/(C_1 p)$ [21]), so for the electrons to gain enough energy to ionize, the electric field needs to be high. For low pressures, the mean free-path will be too long meaning that there would be too little collisions before the electrons are lost, although all the collisions will be ionizing collisions because the electron will have gained enough energy. This results in a vertical asymptote, so that to the left of that asymptote the loss rate is greater than the ionization rate, regardless of the field, because there is not enough molecules to create avalanches.

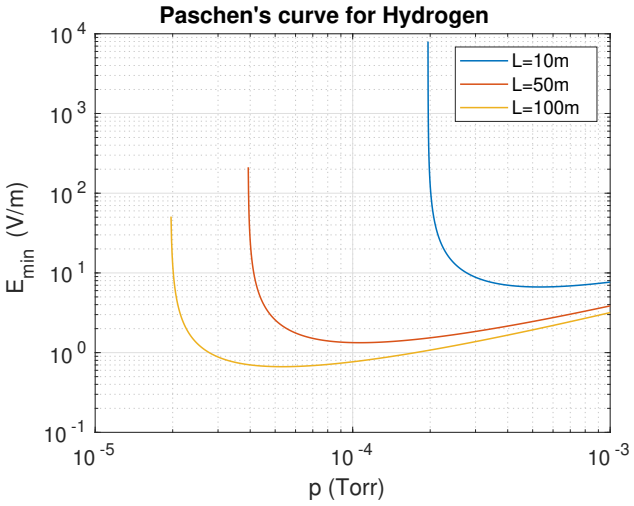

Figure 3.2. Paschen's curve for for H_2 as pre-fill gas, showing different connection lengths.

A widely used empirical criteria for a reliable startup is the so-called Lloyd's criteria [24]

$$E_\varphi \frac{B_\varphi}{B_\theta} > 1000\text{Vm}^{-1}. \tag{3.10}$$

In the case of plasma break-down assisted by Electron Ciclotron Resonance Heating (ECRH), which is a heating method based on the irradiation of electromagnetic waves of certain frequencies to the ionized gas so that it absorbs them helping ionize the gas [19], the minimum value is 100Vm^{-1} instead of 1000Vm^{-1} [26].

In the DIII-D tokamak[3] it has been shown [27] that the break-down of the pre-fill gas did not occur where the stray poloidal field was minimum; instead, it took place where the potential gained by the electrons along their path $\int_{\text{field line}} \vec{E} \cdot \vec{dl}$ was greatest. This potential is not the electrostatic potential because the electric field has been created by a changing magnetic field. An electrostatic field $\vec{E}$ can be written as $\vec{E} = -\nabla V$, where V is the electrostatic potential. The line integral between two points A and B is $\int_A^B \vec{E} \cdot \vec{dl} = -V(B) + V(A)$, so it does not depend on the path followed, only on the starting and ending points. In the presence of transient magnetic fields, the electric field is given by $\vec{E} = -\nabla V - \partial\vec{A}/\partial t$, where $\vec{A}$ is the vector

[3] https://www.ga.com/magnetic-fusion/diii-d.

potential. The line integral in this case would be $\int_A^B \vec{E}\cdot\vec{dl} = \int_A^B -\nabla V\cdot\vec{dl} - \int_A^B \partial\vec{A}/\partial t\cdot\vec{dl} = -V(B)+V(A)-\int_A^B \partial\vec{A}/\partial t\cdot\vec{dl}$. To compute the last integral, the path followed from A to B needs to be known, and hence, the final result will depend on the path followed. This means that an electron gains energy after doing a revolution inside the tokamak returning to the starting point.

The NSTX tokamak[4] also confirms this empirical results [28]. This seems understandable since to create avalanches, the electrons have to gained enough energy to ionize, so it is not only relevant that they follow a path with the minimum deviation to collide as much as possible, but that they gain as much energy as possible in its path so that most of the collisions are ionizing collisions.

3.1.1 Avalanche or break-down time

When Coulomb collisions dominate over neutral-electron collisions, the fuel starts to behave like a plasma, entering the *burn-through* phase. This phase is reached usually when the ionization fraction of the gas is about 5% [19]. At this stage, the avalanche as described above, with a gas being ionized by a toroidal electric field stops being valid, and the further ionization is made by the plasma itself, if the power losses are counterbalanced.

The time when the this phase starts (or when the break-down phase ends) can be estimated using eq (3.7). Introducing the concept of ionization fraction f_i, which is the ratio between the electron density created by ionization and the neutral pre-fill gas density n_{pre}, which is

$$f_i \equiv \frac{n_e/2}{n_{\text{pre}}}, \tag{3.11}$$

where the 2 accounts for the 2 electrons that H_2 (and also He) gives. The pre-fill gas density is related to the gas pressure by the ideal gas law, $p = n_{\text{pre}} K_{\text{B}} T_{\text{pre}}$. Substituting this into (3.7) yields, assuming $n_e(0)$=1 which is an standard assumption [19, 23],

$$f_i(t) = \frac{1}{2n_{\text{pre}}}\exp\left[(\nu_{\text{ion}}-\nu_{\text{loss}})t\right] = \frac{1}{2}\frac{K_{\text{B}}T_{\text{pre}}}{p}\exp\left[v_{\parallel}(\alpha-\frac{1}{L})t\right]. \tag{3.12}$$

Setting $f_i = 5\%$ on (3.12) will give an estimation for the time needed for the avalanche or break-down phase to end, the *avalanche time* t_{ava}:

$$t_{\text{ava}} = \frac{\ln\left(2\cdot 0.05\cdot\dfrac{p}{K_{\text{B}}T_{\text{pre}}}\right)}{v_{\parallel}(\alpha-\dfrac{1}{L})} = \frac{\ln\left(2\cdot 0.05\cdot\dfrac{p}{K_{\text{B}}T_{\text{pre}}}\right)}{43\dfrac{E_\varphi}{p}\left[C_1 p\exp\left(-\dfrac{C_2 p}{E_\varphi}\right)-\dfrac{1}{L}\right]}. \tag{3.13}$$

Note that it is positive since $\alpha - 1/L > 0$ which is the condition for the avalanche to occur.

[4] https://www.pppl.gov/nstx.

3.1.2 Voltage and electric field induced by the inductor solenoid

To start the break-down phase, the inductor solenoid (Sol) is pre-charged with a certain current, and then its current its ramped down rapidly to induce the electric field. In this subsection the electric field and the voltage induced will be derived.

The voltage induced by the ramp down of the Sol, called *loop voltage*, can be easily computed using Faraday's law in its integral form:

$$\varepsilon \equiv V_{\text{loop}} = -\frac{d}{dt}\int_S \vec{B}\cdot\vec{n}dS, \tag{3.14}$$

where S is the surface enclosed by the loop, which is a circle of an arbitrary radius, and $\vec{n}$ its unit vector, which will go in the Z direction. The magnetic field $\vec{B}$ of a solenoid also goes in the Z direction, so the loop voltage is, choosing $\vec{n} = \hat{Z}$:

$$V_{\text{loop}} = -\frac{d}{dt}\int_S B_{\text{Sol}}dS = -\int_S \frac{dB_{\text{Sol}}}{dt}dS. \tag{3.15}$$

The derivative can be introduced into the integral since the integration variables do not vary over time. The only thing that vary with time is the Sol current. Its derivative can be computed easily since the Sol current is decreased linearly, so it satisfies

$$I_{\text{Sol}}(t) = mt + n. \tag{3.16}$$

At $t = 0$, $I_{\text{Sol}} \equiv I_0$, and the ramp goes down until $I_{\text{Sol}}(t_1) \equiv I_1$ $(I_0 > I_1)$, so the Sol current is

$$I_{\text{Sol}}(t) = \frac{I_1 - I_0}{t_1}t + I_0. \tag{3.17}$$

Solving (3.15) for the magnetic field of a solenoid of inner radius R_{in} and outer radius $R_{\text{out}} > R_{\text{in}}$ with N/l turns per unit length, ignoring border effects (i.e., considering infinite length), gives (see appendix A)

$$V_{\text{loop}} = -\mu_0\frac{N}{l}\frac{I_1 - I_0}{t}\left[\pi R_{\text{in}}^2 + \pi(R_{\text{out}}^2 - R_{\text{in}}^2) - \frac{2\pi}{R_{\text{out}} - R_{\text{in}}}\left(\frac{1}{3}(R_{\text{out}}^3 - R_{\text{in}}^3) - \frac{R_{\text{in}}}{2}(R_{\text{out}}^2 - R_{\text{in}}^2)\right)\right]. \tag{3.18}$$

Since the slope of the Sol current is negative, the loop voltage induced is positive.

Once the loop voltage has been computed, the electric field can also be computed. For computing it, the integral form of Faraday's law will be used:

$$V_{\text{loop}} = \varepsilon \equiv \oint_\Gamma \vec{E}\cdot\vec{dl} = -\frac{d}{dt}\int_S \vec{B}\cdot\vec{n}dS, \tag{3.19}$$

where Γ is the loop's perimeter. To compute the electric field $\vec{E}$ from this equation we must know its symmetry. To do so, let's take into account that (3.19) is very similar to Ampère's law

$$\oint_\Gamma \vec{B}\cdot\vec{dl} = \mu_0\int_S \vec{J}\cdot\vec{n}dS = \mu_0 I_{\text{enclosed}}. \tag{3.20}$$

It is widely known that the magnetic field of a infinite cilindral conductor carrying a current density $\vec{J} = J \hat{Z}$ is $\vec{B} = B \overset{\wedge}{\varphi}$ (see any book of classic electromagnetism, like [29]). And, since the roles of $\vec{B}$ and $\vec{J}$ in Ampère's law are the same as the roles of $\vec{E}$ and $\vec{B}$ respectively in Faraday's law, provided that $\vec{B} = B \hat{Z}$ in Faraday's law, the electric field must be $\vec{E} = E \overset{\wedge}{\varphi}$. Furthermore, taking into account the axysymmetry and the assumption of no border effects (infinite length), the electric field can only depend on the radial coordinate R, so $\vec{E} = E(R) \overset{\wedge}{\varphi}$. Considering this, the field can be computed, since $\vec{dl} = Rd\varphi \overset{\wedge}{\varphi}$:

$$V_{\text{loop}} = \oint_{\Gamma} \vec{E} \cdot \vec{dl} = 2\pi R E(R) \Rightarrow E(R) = \frac{V_{\text{loop}}}{2\pi R}. \tag{3.21}$$

The electric field will be more intense near the inner wall of the VV. The same applies to the toroidal magnetic field, which also goes as $1/R$. The potential gained in that region will be the greatest, enhancing the ionization processes, and the magnetic field lines will be mostly toroidal lines in that region (since the toroidal field will be greater in that region, the effect of the poloidal field will be reduced as a consequence), reducing the electron losses. This two factors explain why the pre-fill gas breaks-down near the inner side of the VV in general.

Chapter 4

Fiesta toolbox

The Fiesta toolbox is an object-oriented toolbox programmed in MATLAB by G. Cunningham at the Culham Centre for Fusion Energy [30, 31]. It was created for equilibrium calculations such as solving Grad-Shafranov equation and plasma shape control. However, dynamic calculations are also included, using the RZIp model. The reactor geometry is introduced using its object architecture.

4.1 Grad-Shafranov solver, EFIT

Fiesta contains what is called *free boundary equilibrium solvers*. The main characteristic of this type of solvers is that the plasma boundary is not known (on the contrary of fixed boundary problems) and hence will also be part of the solution. The poloidal magnetic flux ψ is divided into two components, the created by the plasma and the created by the external current carrying elements, i.e., the coils and the VV, which will carry eddy currents. This external elements will be called *structrure*.

The Grad-Shafranov equation is solved by an iterative method, according to a given tolerance. In particular, we have used the EFIT solver [32], which is a free-boundary equilibrium solver that can obtain the external currents needed to achieve a plasma equilibrium with plasma parameters closer to the desired plasma parameters. The plasma current profile used is defined by the so-called Topeol2 model,

$$\begin{cases} \dfrac{dp}{d\psi} = \dfrac{j_0}{r_0}\beta_\theta(1-\psi_\mathrm{N}), \\ f\dfrac{df}{d\psi} = \mu_0 r_0 j_0(1-\beta_\theta)(1-\psi_\mathrm{N}), \end{cases} \tag{4.1}$$

where r_0 is the X-point radial coordinate, j_0 the plasma current and ψ_N the normalized flux,

defined as

$$\psi_{\mathrm{N}} \equiv \frac{\psi - \psi_{\mathrm{axis}}}{\psi_{\mathrm{boundary}} - \psi_{\mathrm{axis}}}, \tag{4.2}$$

where ψ_{axis} and ψ_{boundary} are the values of the poloidal flux at the center of the magnetic flux surface and at its boundary respectively. The constants r_0 and j_0 are adjusted at each step of the iterative process. The field and the flux at the computational grid are calculated using Green's functions (see [33] for a review of the Green's function formalism applied to tokamaks).

4.2 RZIp model

The rigid current displacement model or RZIp (R, Z and I_{p}) [34, 35] is a model used to describe the dynamic behaviour of a tokamak equilibrium. The plasma is modelled as a rigid conductor so that the plasma can move radially and vertically, but the plasma shape and current distribution remain constant. Hence, the plasma can be identified by its radial and vertical position, R_{geo} and Z_{geo}, and its current, I_{p}. The RZIp model is a linearised model based on the assumption that small perturbations leads to small changes of the target equilibrium. Its equations are the circuit equation and the radial and vertical force balance equations.

This model considers that a tokamak is made of active and passive elements. An element is considered an active element if is subjected to a external excitation such as current or voltage supplies and passive in any other case. The active structure will then be the coilset, and the passive structure the vacuum vessel.

There are several ways of calculate the plasma self-inductance. Fiesta's RZIp uses this approximate formula [35]

$$L_{\mathrm{p}} = \mu_0 R_{\mathrm{geo}} \Big(4\pi R_{\mathrm{geo}} \frac{| < B_{Z_{\mathrm{p}}} > |}{\mu_0 I_{\mathrm{p}} - \beta_\theta} - \beta_\theta - \frac{1}{2} \Big), \tag{4.3}$$

where $B_{Z_{\mathrm{p}}}$ is the B_Z created by the plasma (in our case, the plasma current flows in the positive toroidal direction, resulting in a negative $< B_{Z_{\mathrm{p}}} >$).

The four equations of the RZIp model are, indicating matrices with bold letters [34]

$$\frac{d(L_{\mathrm{p}} I_{\mathrm{p}} + \boldsymbol{M_{ps}} \boldsymbol{I}_{\mathrm{s}} + R_{\mathrm{Geo}} \boldsymbol{E} I_p)}{dt} + I_{\mathrm{p}} \rho_{\mathrm{p}} = V_{\mathrm{p}} \ [I_{\mathrm{p}} \text{ equation}], \tag{4.4}$$

$$\frac{d(\boldsymbol{L}_{\mathrm{s}} \boldsymbol{I}_{\mathrm{s}} + \boldsymbol{M}_{\mathrm{sp}} I_{\mathrm{p}})}{dt} + \boldsymbol{\Omega}_{\mathrm{s}} \boldsymbol{I}_{\mathrm{s}} = \boldsymbol{V}_{\mathrm{s}} \ [\boldsymbol{I}_{\mathrm{s}} \text{ equation}], \tag{4.5}$$

$$\frac{d(m_{\mathrm{p}} \dot{R}_{\mathrm{geo}})}{dt} = \frac{1}{2} I_{\mathrm{p}}^2 \frac{\partial L_{\mathrm{p}}}{\partial R_{\mathrm{geo}}} + \boldsymbol{I}_{\mathrm{s}} \frac{\partial \boldsymbol{M}_{\mathrm{sp}}}{\partial R_{\mathrm{geo}}} I_{\mathrm{p}} + \frac{\boldsymbol{E} I_{\mathrm{p}}^2}{2} \ [R_{\mathrm{geo}} \text{ equation}], \tag{4.6}$$

$$\frac{d(m_{\mathrm{p}} \dot{Z}_{\mathrm{geo}})}{dt} = \boldsymbol{I}_{\mathrm{s}} \frac{\partial \boldsymbol{M}_{\mathrm{sp}}}{\partial Z_{\mathrm{geo}}} I_{\mathrm{p}} \ [Z_{\mathrm{geo}} \text{ equation}], \tag{4.7}$$

where $\boldsymbol{E}$ is a constant matrix, $\boldsymbol{M}_{\mathrm{ps}}$ is the inductance between the plasma and the structure (both active and passive), $\boldsymbol{I}_{\mathrm{s}}$ the current of the structure, $\boldsymbol{V}_{\mathrm{s}}$ and V_{p} the voltage of the structure and the plasma respectively and $\boldsymbol{\Omega}_{\mathrm{s}}$ the resistance matrix of the structure. Is is common to neglect the plasma mass m_p, which is also what Fiesta's RZIp does. This set of equations are linearized and cast in the state space form to solve it, whose general structure is (see appendix B)

$$\begin{cases} \dfrac{d\boldsymbol{x}}{dt} = \boldsymbol{A}\boldsymbol{x} + \boldsymbol{B}\boldsymbol{u}, \\ \boldsymbol{y} = \boldsymbol{C}\boldsymbol{x} + \boldsymbol{D}\boldsymbol{u}. \end{cases} \tag{4.8}$$

The linearizations of eq (4.4), (4.5), (4.6) and (4.7) setting $m_p = 0$ result in:

$$\begin{bmatrix} \boldsymbol{L}_{\mathrm{s}} & \dfrac{\partial \boldsymbol{M}_{\mathrm{ps}}}{\partial Z_{\mathrm{geo}}}\Big|_0 \\ \dfrac{\partial \boldsymbol{M}_{\mathrm{ps}}}{\partial Z_{\mathrm{geo}}}\Big|_0 & \dfrac{\partial^2 \boldsymbol{M}_{\mathrm{ps}}}{\partial Z_{geo}^2}\Big|_0 \dfrac{\boldsymbol{I}_{\mathrm{s}}{}^0}{I_{\mathrm{p}}^0} \\ \dfrac{\partial \boldsymbol{M}_{\mathrm{ps}}}{\partial R_{\mathrm{geo}}}\Big|_0 & \dfrac{\partial^2 \boldsymbol{M}_{\mathrm{ps}}}{\partial Z_{\mathrm{geo}}\partial R_{\mathrm{geo}}}\Big|_0 \dfrac{\boldsymbol{I}_{\mathrm{s}}{}^0}{I_{\mathrm{p}}^0} \\ \boldsymbol{M}_{\mathrm{ps}} & 0 \end{bmatrix}$$

$$\begin{bmatrix} \dfrac{\partial \boldsymbol{M}_{\mathrm{sp}}}{\partial R_{\mathrm{geo}}}\Big|_0 & \boldsymbol{M}_{\mathrm{ps}}{}^0 \\ \dfrac{\partial^2 \boldsymbol{M}_{\mathrm{ps}}}{\partial R_{\mathrm{geo}}\partial Z_{\mathrm{geo}}}\Big|_0 \dfrac{\boldsymbol{I}_{\mathrm{s}}{}^0}{I_{\mathrm{p}}^0} & 0 \\ \dfrac{1}{2}\dfrac{\partial^2 L_{\mathrm{p}}}{\partial R_{\mathrm{geo}}^2}\Big|_0 + \dfrac{\partial^2 \boldsymbol{M}_{\mathrm{ps}}}{\partial R_{\mathrm{geo}}^2}\Big|_0 \dfrac{\boldsymbol{I}_{\mathrm{s}}{}^0}{I_{\mathrm{p}}^0} & \dfrac{\partial L_{\mathrm{p}}}{\partial R_{\mathrm{geo}}}\Big|_0 + \dfrac{\partial \boldsymbol{M}_{\mathrm{ps}}}{\partial R_{\mathrm{geo}}}\Big|_0 \dfrac{\boldsymbol{I}_{\mathrm{s}}{}^0}{I_{\mathrm{p}}^0} + \mu_0 \dfrac{2\pi S}{l^2}\beta_p R_{\mathrm{geo}}^0 \\ \dfrac{\partial L_{\mathrm{p}}}{\partial R_{\mathrm{geo}}}\Big|_0 + \dfrac{\partial \boldsymbol{M}_{\mathrm{ps}}}{\partial R_{\mathrm{geo}}}\Big|_0 \dfrac{\boldsymbol{I}_{\mathrm{s}}{}^0}{I_{\mathrm{p}}^0} + \mu_0 \dfrac{2\pi S}{l^2}\beta_p R_{\mathrm{geo}}^0 & L_{\mathrm{p}}^0 + \mu_0 \dfrac{2\pi S}{l^2}\beta_p R_{\mathrm{geo}}^0 \end{bmatrix} * \frac{d\boldsymbol{x}}{dt} + \tag{4.9}$$

$$+ \begin{bmatrix} \boldsymbol{\Omega}_{\mathrm{s}}^{\boldsymbol{0}} & 0 & 0 & 0 \\ 0 & 0 & 0 & 0 \\ 0 & 0 & 0 & 0 \\ 0 & 0 & 0 & \Omega_{\mathrm{p}}^0 \end{bmatrix} \boldsymbol{x} = \begin{bmatrix} \boldsymbol{I} & 0 \\ \boldsymbol{0} & 0 \\ \boldsymbol{0} & 0 \\ \boldsymbol{0} & 1 \end{bmatrix} \begin{bmatrix} \delta \boldsymbol{V}_{\mathrm{s}} \\ \delta V_{\mathrm{p}} \end{bmatrix},$$

where ^{0} indicates equilibrium value, so R_{geo}^0 indicates the value at the target equilibrium, S is

the plasma cross-section of the equilibrium configuration, and l its perimeter. The state vector $\boldsymbol{x}$ is

$$\boldsymbol{x} = \begin{bmatrix} \boldsymbol{I}_{\mathrm{s}} - \boldsymbol{I}_{\mathrm{s}}{}^{0} \\ (Z_{\mathrm{geo}} - Z^{0}_{\mathrm{geo}})I^{0}_{\mathrm{p}} \\ (R_{\mathrm{geo}} - R^{0}_{\mathrm{geo}})I^{0}_{\mathrm{p}} \\ I_{\mathrm{p}} - I^{0}_{\mathrm{p}} \end{bmatrix} = \begin{bmatrix} \delta(\boldsymbol{I}_{\mathrm{s}}) \\ \delta(Z_{\mathrm{geo}})I^{0}_{\mathrm{p}} \\ \delta(R_{\mathrm{geo}})I^{0}_{\mathrm{p}} \\ \delta(I_{\mathrm{p}}) \end{bmatrix}. \tag{4.10}$$

and the input vector $\boldsymbol{u}$ is

$$\boldsymbol{u} = \begin{bmatrix} \delta\boldsymbol{V}_{\mathrm{s}} \\ \delta V_{\mathrm{p}} \end{bmatrix}. \tag{4.11}$$

However, Fiesta's RZIp do not uses the voltages as inputs, it uses the coilset currents as inputs, so (4.9) is inverted to have currents as inputs. The system (4.9) has the form $\boldsymbol{M}\frac{d\boldsymbol{x}}{dt} + \boldsymbol{P}\boldsymbol{x} = \boldsymbol{Q}\boldsymbol{u}$, and comparing it with the state space system (4.8), we conclude

$$\begin{aligned} \boldsymbol{A} &= -\boldsymbol{M}^{-1}\boldsymbol{P}, \\ \boldsymbol{B} &= \boldsymbol{M}^{-1}\boldsymbol{Q}. \end{aligned} \tag{4.12}$$

The self and mutual inductances on (4.9) are computed with the Green's functions of the magnetic field by relating them to the field created by the structure and by the plasma. Using (2.11) and the division of the flux into the created by the plasma and the created by the structure:

$$\begin{gathered} \psi = \psi_{\mathrm{p}} + \psi_{\mathrm{s}} \quad , \\ B_R = B_{R_{\mathrm{p}}} + B_{R_s}, \quad B_Z = B_{Z_{\mathrm{p}}} + B_{Z_s}, \\ B_{R_{\mathrm{p}}} = \frac{-1}{R}\frac{\partial\psi_{\mathrm{p}}}{\partial Z}, \qquad B_{R_s} = \frac{-1}{R}\frac{\partial\psi_{\mathrm{s}}}{\partial Z}, \\ B_{Z_{\mathrm{p}}} = \frac{1}{R}\frac{\partial\psi_{\mathrm{p}}}{\partial R}, \qquad B_{Z_{\mathrm{s}}} = \frac{1}{R}\frac{\partial\psi_{\mathrm{s}}}{\partial R}. \end{gathered} \tag{4.13}$$

The output vector $\boldsymbol{y}$ contains the state vector variables and diagnostic measurements such as the poloidal field or flux measurements. In our case, we only use poloidal field measures so

the output vector is

$$\boldsymbol{y} = \boldsymbol{C}\boldsymbol{x} \Rightarrow \begin{bmatrix} \delta(\boldsymbol{I}_{\mathrm{s}}) \\ \delta(Z_{\mathrm{geo}})I_{\mathrm{p}}^{0} \\ \delta(R_{\mathrm{geo}})I_{\mathrm{p}}^{0} \\ \delta(I_{\mathrm{p}}) \\ B_{\theta_n} \end{bmatrix} = \tag{4.14}$$

$$= \begin{bmatrix} \boldsymbol{I} & 0 & 0 & 0 \\ \boldsymbol{0} & 1 & 0 & 0 \\ \boldsymbol{0} & 0 & 1 & 0 \\ \boldsymbol{0} & 0 & 0 & 1 \\ \dfrac{\partial(\vec{B}\cdot\vec{n})_n}{\partial \boldsymbol{I}_{\mathrm{s}}} & \dfrac{\partial(\vec{B}\cdot\vec{n})_n}{\partial(\delta(Z_{\mathrm{Geo}})I_{\mathrm{p}}^{0})} & \dfrac{\partial(\vec{B}\cdot\vec{n})_n}{\partial(\delta(R_{\mathrm{Geo}})I_{\mathrm{p}}^{0})} & \dfrac{\partial(\vec{B}\cdot\vec{n})_n}{\partial I_{\mathrm{p}}} \end{bmatrix} \begin{bmatrix} \delta(\boldsymbol{I}_{\mathrm{s}}) \\ \delta(Z_{geo})I_{\mathrm{p}}^{0} \\ \delta(R_{geo})I_{\mathrm{p}}^{0} \\ \delta(I_{\mathrm{p}}) \end{bmatrix},$$

where the subscript n in the poloidal field B_θ indicates the measure n, and $\vec{n}$ is the normal vector of the loop that measures the poloidal field [34] (section 3.3). The feed-forward matrix $\boldsymbol{D}$ is zero provided that there is no direct relation between the inputs and the outputs.

Using (4.14), the coil currents needed to obtain poloidal field null in the region where the sensors are placed (null currents) can be computed by simply setting to zero the elements of $\boldsymbol{y}$ related to the field, and computing the coil currents needed, using only the coil currents in $\boldsymbol{x}$, and the corresponding elements of the $\boldsymbol{C}$ matrix. This is crucial for the break-down phase, since the poloidal field has to be null out as much as possible to ensure the Townsend avalanche.

The system (4.9) is solved by a Runge-Kutta adaptive method (function ode45 from MATLAB), obtaining the time evolution of the plasma current, the eddy currents in the vacuum vessel and the coilset and plasma voltages, given the current profile of the coilset. As stated previously, RZIp is a perturbative model on an equilibrium state. This equilibrium configuration have been obtained with the Grad-Shafranov solver of Fiesta, so RZIp is applied after the equilibrium configuration is obtained.

Fiesta is a complex toolbox, of thousands of code lines, and it is scarcely documented, so direct code reading is imperative. However, for this thesis is sufficient to understand the basis of the Fiesta toolbox as described above. Figure 4.1 shows a flow diagram of the Fiesta toolbox as it has been used.

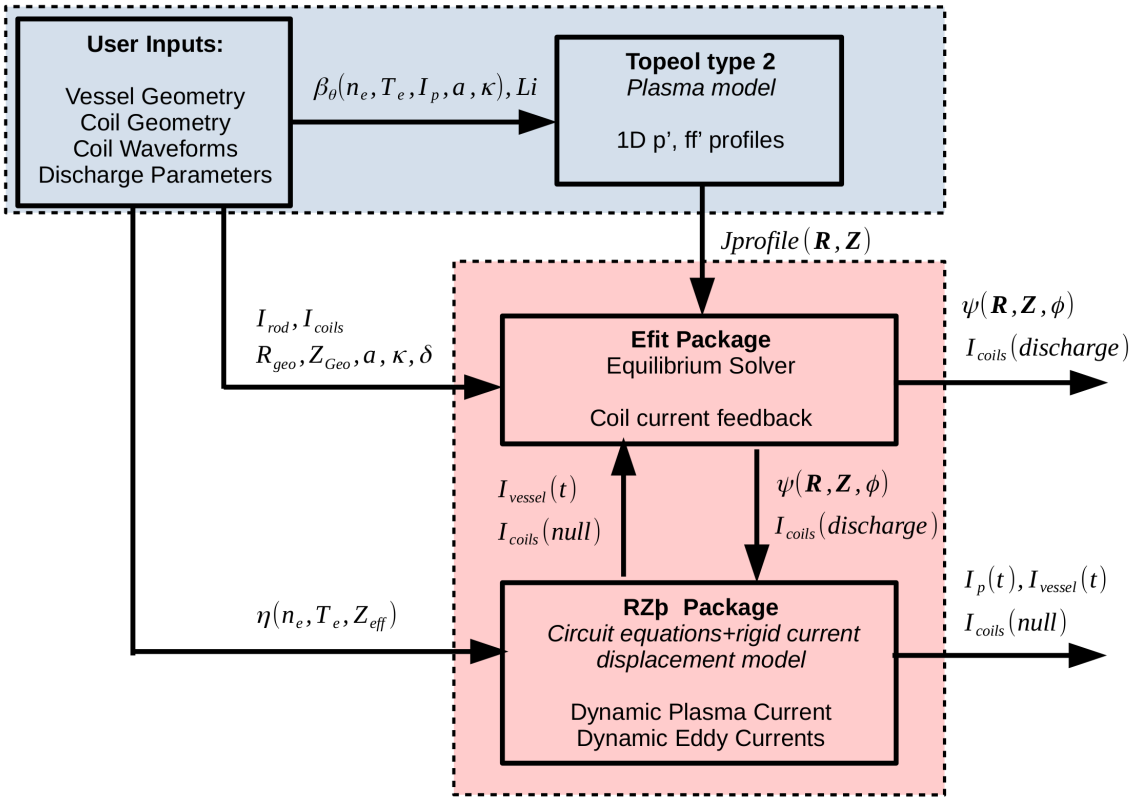

Figure 4.1. Flow diagram of the Fiesta toolbox. Source: [36].

Chapter 5

Simulation procedure

To study the break-down conditions for the SMART reactor, the Paschen's curve and the estimation avalanche time have been calculated, as well as an study of the electromagnetic fields and derived variables such as the connection length, the potential gained by the electrons and the empirical Lloyd's criteria. The Fiesta toolbox have been used to compute the magnetic fields.

This thesis have been developed during the design phase of the SMART tokamak, maturing through discussions within the team and within other teams such as the korean VEST team and the company Tokamak Energy (Culham, UK). The changes in the coilset were specially delicate since the same plasma equilibrium configuration had to be achieved. Part of the work carried out also contributed to this changes, but the main focus was the study of the break-down conditions for each configuration. The work included here are the most updated configurations for both the first operational phase, phase 1, and a future update, phase 2[1]. A plot of the cross-section and the 3D plot of the SMART reactor done with Fiesta is included on figure 5.1. Note the VV implemented is simpler than the more realistic VV showed on figure 1.10. There is no toroidal field coils because Fiesta assumes axisymmetry so the toroidal magnetic field is given as an input to Fiesta.

The final configuration of the coilset have been chosen so that it allows highly shaped plasmas, such has having plasmas with negative triangularities. The coils are also named on figure 5.1, from the inductor Solenoid, Sol, to the poloidal field coils PF1 and PF2 and the divertor coils Div1 and Div2.

A crucial criteria for setting the coilset currents has been the achievement of the break-down of the pre-fill gas, without any assistance method (heating methods), only by using the

[1]Note for the SMART team: this are S1-19 and S2-16 baseline cases.

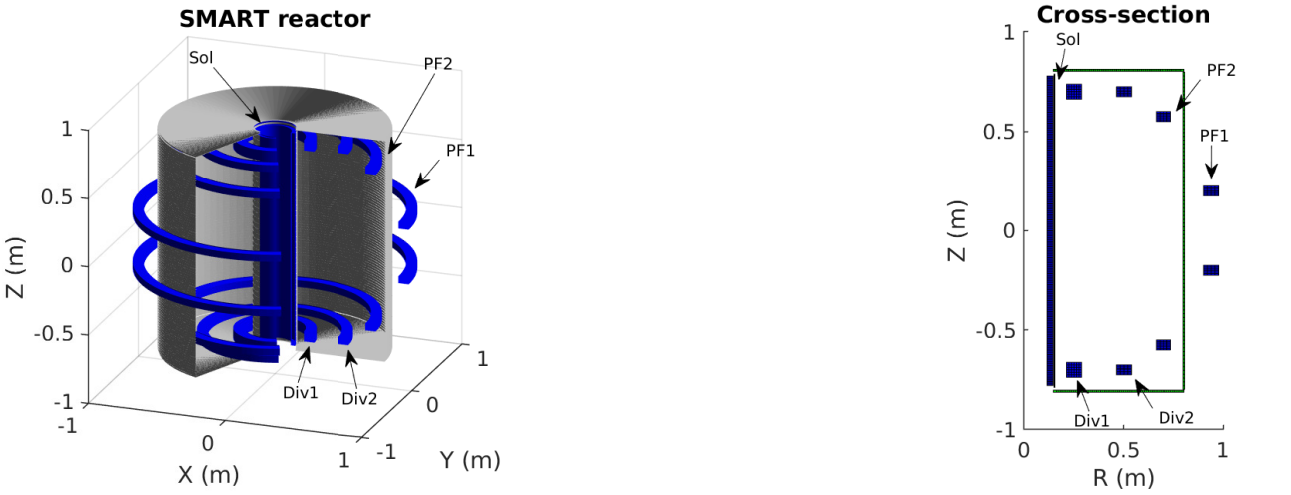

(a) 3D plot of SMART.

(b) Cross-section of SMART.

Figure 5.1. Plot of the SMART reactor implemented on Fiesta. There is symmetry with respect to the $Z = 0$ plane. There is no toroidal field coils because Fiesta assumes axysymmetry. The toroidal field is given as an input.

Sol coil (*ohmic break-down*). To confirm this, the criteria explained on section 3.1, such as the Paschen's curve, the empirical LLoyd's criteria and the estimation of the avalanche time have been applied. The avalanche time should be as short as possible, so that the avalanche phase ends rapidly. Other tokamaks show break-down times between 1 and 4ms [37, 28]. Similar values have been attempted. H_2 have been used as a pre-fill gas. The electric field and loop voltage induced by the solenoid have been calculated analytically using the equations showed on section 3.1.2.

The currents during the break-down phase, from the ramping up of the Sol to the end of this phase have been calculated from RZIp (currents needed to null out the poloidal field or *null currents*), while the currents during the target equilibrium and the sustaining of this equilibrium were given as an input (the coil current waveforms will be explained in chapter 6). With the full current waveforms, the fields at the break-down phase, Lloyd's criteria and the connection length have been studied. With the connection length, the Paschen's curve and the avalanche time was checked to test whether ohmic break-down was possible or not.

The break-down conditions have been studied at t=0ms, just when the Sol induced the electric field that will ionize the gas, so there is no plasma's magnetic field, only the structure's magnetic fields (eddy currents in the VV+coilset currents). For additional safety, I also added the Earth's field[2]; the field added is

[2]The Earth's field have been computed from https://www.ngdc.noaa.gov/geomag/calculators/magcalc.shtml, using IGRF model, and averaging the R and ϕ component to have an axysymmetric value, so it can be

$$\left.\begin{aligned} B_{\mathrm{R}} &= 2.7 \cdot 10^{-7}\mathrm{T}, \\ B_{\mathrm{Z}} &= -3.38 \cdot 10^{-5}\mathrm{T}, \end{aligned}\right\} \Leftrightarrow B_\theta = 3.38 \cdot 10^{-5}\mathrm{T}. \tag{5.1}$$

This addition ensures the poloidal field obtained inside the VV is never lower than the Earth's field, since in reality, the field will be larger than Earth's field, and also there will be other issues increasing the field such as errors on the coils winding or magnetic materials surrounding the reactor.

5.1 Field line tracer

To compute the connection length by field line tracing, a field line tracer function was made. The field lines of a vector field are always tangent to the vector field. If the diferential vector $\vec{dr}$ lies in the field lines of a vector field $\vec{B} = \vec{B}(R, Z)$ (independent on the φ angle due to the axisymmetry), $\vec{dr}$ will always be paralell to $\vec{B}(R, Z)$, so

$$\vec{B} \parallel \vec{dr} \Rightarrow \vec{B} \wedge \vec{dr} = 0 \Rightarrow \quad \frac{B_\varphi(R,Z)}{R d\varphi} = \frac{B_Z(R,Z)}{dZ} = \frac{B_R(R,Z)}{dR} \equiv \text{constant}, \tag{5.2}$$

To integrate (5.2), the toroidal angle φ has been chosen as independent variable since it is always positive and monotically increasing, leaving R, Z as the dependent variables. The equations to solve are

$$\left.\begin{aligned} \frac{dR}{d\varphi} &= R(\varphi)\frac{B_R(R(\varphi),Z(\varphi))}{B_\varphi(R(\varphi),Z(\varphi))} \\ \frac{dZ}{d\varphi} &= R(\varphi)\frac{B_Z(R(\varphi),Z(\varphi))}{B_\varphi(R(\varphi),Z(\varphi))} \end{aligned}\right\} \tag{5.3}$$

The total (poloidal and toroidal) length of the magnetic field line is

$$\begin{aligned} ds^2 = dR^2 + (Rd\varphi)^2 + dZ^2 \Rightarrow \\ \frac{ds}{d\varphi} = R(\varphi)\sqrt{1 + \left(\frac{B_R(R(\varphi),Z(\varphi))}{B_\varphi(R(\varphi),Z(\varphi))}\right)^2 + \left(\frac{B_Z(R(\varphi),Z(\varphi))}{B_\varphi(R(\varphi),Z(\varphi))}\right)^2} = \\ = R(\varphi)\sqrt{1 + \frac{B_\theta(R(\varphi),Z(\varphi))^2}{B_\varphi(R(\varphi),Z(\varphi))^2}} \end{aligned} \tag{5.4}$$

Equations (5.3) and (5.4) can be easily integrated with MATLAB using the ODE function. The initial value of φ has been set as $\varphi_0 = 0$. The initial R and Z values have been varied so that lines starting through all of the VV are followed. The range of φ has been chosen so that all the lines end up colliding with the inner walls of the VV or with the coils inside the VV. The final value of the magnetic field length will be the connection length L

introduced on Fiesta. The values correspond to the values of 3/4/2020.

Nevertheless, due to computer demands, (5.3) and (5.4) have been integrating using the poloidal length l_θ:

$$\vec{B} \parallel \vec{dr} \Rightarrow \vec{B} \wedge \vec{dr} = 0 \Rightarrow \frac{B_\varphi(R,Z)}{Rd\varphi} = \frac{B_\theta(R,Z)}{dl_\theta} \equiv \text{constant} \Rightarrow \frac{d\varphi}{dl_\theta} = \frac{1}{R}\frac{B_\varphi(R,Z)}{B_\theta(R,Z)} \tag{5.5}$$

Introducing that change of variable on (5.3) and (5.4), now $R, Z = R(l_\theta), Z(l_\theta)$ and $\varphi = \varphi(l_\theta)$ is also a dependent variable, and the equations to solve are

$$\left.\begin{aligned} \frac{d\varphi}{dl_\theta} &= R(l_\theta)\frac{B_\varphi(R(l_\theta),Z(l_\theta))}{B_\theta(R(l_\theta),Z(l_\theta))} \\ \frac{dR}{dl_\theta} &= \frac{B_R(R(l_\theta),Z(l_\theta))}{B_\theta(R(l_\theta),Z(l_\theta))} \\ \frac{dZ}{dl_\theta} &= \frac{B_Z(R(l_\theta),Z(l_\theta))}{B_\theta(R(l_\theta),Z(l_\theta))} \\ \frac{ds}{dl_\theta} &= \sqrt{1+\frac{B_\varphi(R(l_\theta),Z(l_\theta))^2}{B_\theta(R(l_\theta),Z(l_\theta))^2}} \end{aligned}\right\} \tag{5.6}$$

5.1.1 Potential

As commented on section 3.1, one effective criteria to estimate where do break-down takes place is to compute the potential function (which is not the electrostatic potential, as commented on the cited section) gained by the electron as it travels along a magnetic field line:

$$U = \int_{\text{field line}} \vec{E}\cdot\vec{dl} = \int_{\text{field line}} E_\varphi R d\varphi \simeq \int_{\text{field line}} E_\varphi ds = \int_{\text{field line}} \frac{V_{\text{loop}}}{2\pi R} ds, \tag{5.7}$$

where ds is the total (poloidal and toroidal) differential length of the field line, which has been approximated, as usual, as the toroidal length of the line.

The non-dimensional magnitude U/V_{loop} has been computed [27]. To calculate it, (5.7) have been re-written as an ODE, so it can also be integrated with MATLAB:

$$\frac{d(U/V_{\text{loop}})}{ds} = \frac{1}{2\pi R} \Rightarrow \frac{d(U/V_{\text{loop}})}{dl_\theta} = \frac{d(U/V_{\text{loop}})}{ds}\frac{ds}{dl_\theta} = \frac{1}{2\pi R(l_\theta)}\frac{ds}{dl_\theta}. \tag{5.8}$$

Zero has been set as initial value of U/V_{loop}.

Chapter 6

Results

In this chapter the main physics results of this thesis are described and discussed. The first section included the coilset currents, the target equilibrium and the time evolution of the plasma current and the eddy currents in the vacuum vessel. The second section includes the study of the break-down scenario, including the magnetic fields at the beginning of the break-down phase, the connection length and the electric potential gained by an electron following the field lines, and finally the Paschen's curve and the calculation of the avalanche time. The third section includes a discussion of the results with other tokamaks.

6.1 Static and dynamic behaviour of SMART

In this first section, the target equilibrium, the current waveforms and the time evolution of the plasma current and the eddy currents in the vacuum vessel are shown for phase 1 and 2, obtained with the Fiesta toolbox. This results will later be used for the break-down study.

6.1.1 Target equilibrium

Figure 6.1 includes the target equilibrium of both phases, indicating the poloidal flux with a colorbar, being the flux maximum at the magnetic axis. Both plots displays 3 bulk regions (upper, central and lower). The central bulk region correspond to the plasma, while the others are created by the divertor coils and have no plasma since they collide with the wall. The plasma is a diverted plasma with two X-points, due to the symmetry with respect to the $Z = 0$ plane. VV's eddy currents are not included here because RZIp do not allow that the equilibrium configuration have eddy currents.

Tables 6.1 and 6.2 includes the coil currents and the main plasma parameters. Both plasmas

displays positive triangularities, about 0.2, although plasmas with negative triangularities can also be obtained with the same coilset configuration if the PF2 coils act as divertor coils, so that they take the role of the Div1 coils, and upper and lower bulks will be placed on the PF2 coils instead of on Div1. The parameters $q0$ and $q95$ are the safety factor at a surface with Ψ_N =0 and 0.95 respectively (Ψ_N is zero for the magnetic axis, and 1 for the plasma boundary or separatrix). Div2 current is zero in the target equilibrium because Div2 is only used in the break-down phase.

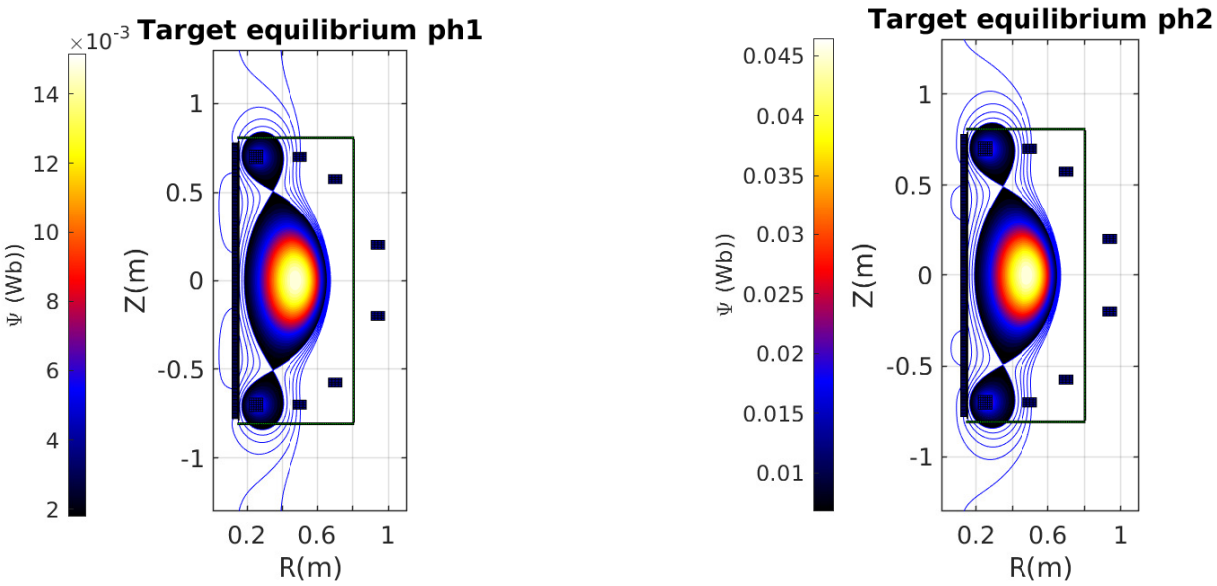

(a) Phase 1.

(b) Phase 2.

Figure 6.1. Target equilibrium for both phases, showing the coil currents for the equilibrium configuration and several plasma parameters at the right. 3 bulk region are showed on both plots (upper, lower and central), being the plasma in the central bulk. The colorbar indicates the poloidal flux Ψ. Eddy currents in the VV are not included here.

6.1.2 Current waveforms

As stated on chapter 5, the current waveforms were given as an input lacking on the currents during the break-down, which were calculated using RZIp.

Previous to the RZIp simulation, the region where the poloidal field will be nulled out (poloidal null region) had to be chosen. The size and location was optimized manually to maximize the empirical connection length (3.5) and reducing the current needed to create the null region. The best shape and size are the one showed on figure 6.2, an square of 0.30x0.30m^2 centered at $R_{\text{null}} = 0.31$m. The sensors, or magnetic field probes are shown. The region is placed close to the inner wall since its near the inner wall where the gas breaks-down, as explained on

Coil	I(kA)	
	Phase 1	Phase 2
Sol	-0.15	-0.30
PF1	-0.47	-1.49
PF2	-0.07	-0.14
Div1	0.30	1.00
Div2	0.00	0.00

Table 6.1. Coilset currents for the target equilibrium configuration for both phases. Div2 current is zero because it is used only for the break-down phase.

Parameter	Phase 1	Phase 2
R_{geo}(m)	0.42	0.42
A	1.82	1.84
κ	1.95	2.01
δ	0.20	0.24
q0	1.14	1.03
q95	7.23	7.02
$\beta_\varphi(\%)$	2.92	3.71
β_θ	0.73	0.91
$\beta_{\text{N}}(\%)$	1.98	2.56

Table 6.2. Plasma parameters on the target equilibrium for both phases. Z_{geo}=0 due to the symmetry with respect t the $Z = 0$ plane.

section 3.1.

The full current waveforms, after computing the current needed to null out as much as possible the poloidal field in the sensor region with RZIp, is showed on figure 6.3. This figure also includes the current gradient at each time, which will be denoted with Δ. Each current waveform have 7 dots indicating the phases of the plasma discharge, as indicated in figure 6.3 (b):

- Point 1, the starting point: all the currents are zero.
- Point 2, pre-pulse: the Sol coil is charged, and the PF and Div coils are ramped on to the currents needed to null out the poloidal field created by the Sol (null currents).
- Point 3, 1^{o} ramp-down: at this point, t=0ms, the Sol current is ramped down, inducing the loop voltage that will ionize the pre-fill gas. The PF and Div coils are the null currents to null out the poloidal field so the avalanche can succeed.
- Point 4, 2^{o} ramp-down: at this point, the Sol coil change its decreasing slope to make it less abrupt. The PF and Div coil currents are still the null currents. The break-down of the pre-fill gas will happen between point 3 and 4. The time interval between them was fixed to match the avalanche time.
- Point 5, target equilibrium: at this point the target equilibrium is reached. The PF and Div coil currents are the values at the target equilibrium.

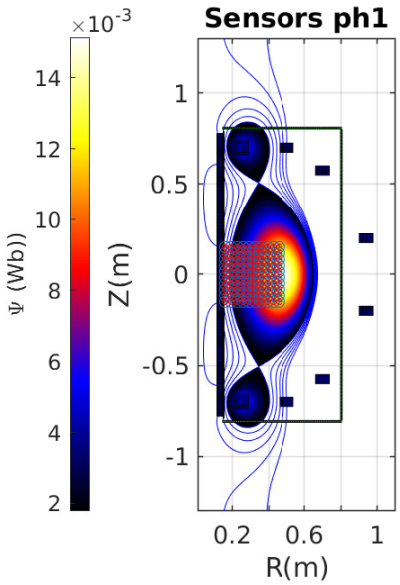

Figure 6.2. Sensors for the poloidal null region. In that region the poloidal magnetic field will be nulled out (as much as possible) by the PF and Div coils.

- Point 6, end target equilibrium: the target equilibrium is sustained from point 5 to point 6, being the time interval between them the *flat-top time*, which is 20ms on phase 1 and 100ms on phase 2. The Sol coil current vary so that the desired plasma current is maintained, while the PF and Div currents are kept constant

- Point 7, termination of the plasma discharge: all the coil currents are turned off, ending the plasma discharge.

To model the plasma current, Spitzer's resistivity have been used, using $Z_{eff} = 2$ as effective atomic number to account for Carbon impurities because the plasma-facing material in SMART will be Carbon. Due to the low resistivity on phase 1, the Sol current has to increase from point 5 to 6 to prevent further increase of the plasma current.

The Sol waveform have 2 decreasing slopes, the first one with a higher slope to induce the electric field and the following with a lower slope to continue increasing the plasma current but at a lower rate. The reason for this two slopes is because of engineering requirements. With the design of the power supplies for phase 1, the first operational phase, the coilset current gradients could not surpass 50A/ms. But this slope was not enough to allow the break-down of the pre-fill gas (the electric field induced was below the paschen's curve, so break-down was not possible, the loss rate were greater than the ionization rate), so finally it was decided that there would be a first slope to induce the loop voltage that would surpass the operational limits and would be sustained until the break-down phase ends, and another slope within the operational limits once the break-down phase was finished. Note that the rest of the ramp currents for

phase 1 are below 50A/ms. The time interval between point 1 and 2 was chosen so that the current ramp is lower than 50A/ms. The second slope was designed so that the plasma current rises up at rate from 1 to 10MA/s, as was found in spherical tokamaks with ohmic startup [27, 38, 39, 40]. The above discussion applies to phase 1 only, but phase 2 was also built with two slopes since this two slopes Sol waveform is less demanding for the power supplies.

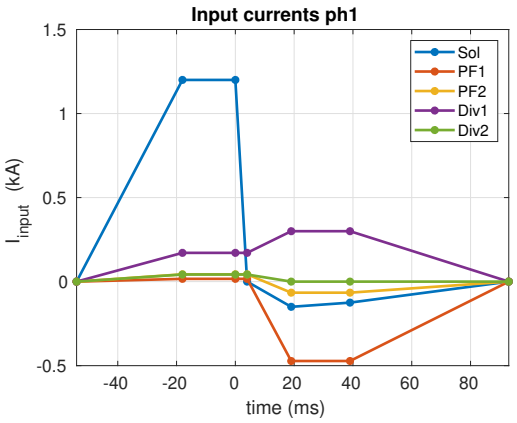

(a) Input currents of phase 1.

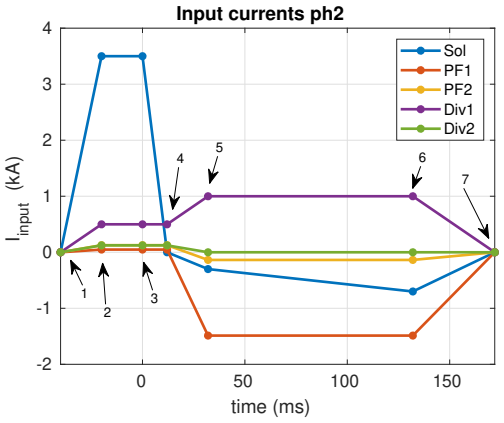

(b) Input currents of phase 2, indicating the discrete points of each of the waveforms.

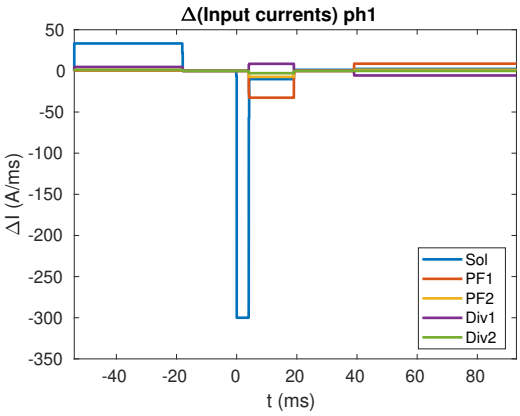

(c) Currents gradients of phase 1.

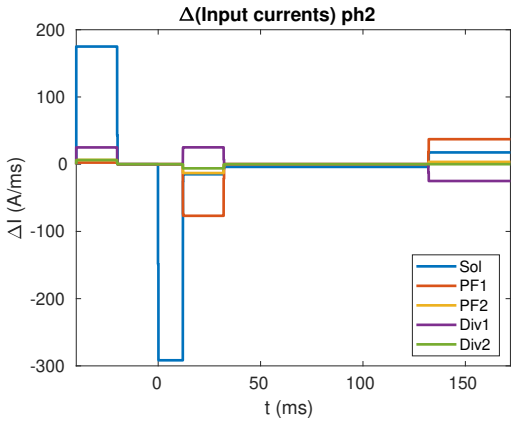

(d) Currents gradients of phase 2.

Figure 6.3. Coilset currents given as inputs and current gradients for both phases. The desired plasma current is sustained for 20ms in phase 1 and for 100ms in phase 2 (flat-top time).

6.1.3 Dynamic simulations

The RZIp outputs, the plasma current and the net eddy current induced in the VV as a function of time are shown on figure 6.4. The coil waveforms have also been included for a better understanding of the outputs. Regarding the plasma current, it can be seen the different growth rate of it due to the 2 slopes of the Sol current, being the first one more abrupt. The plasma is sustained for the desired time, 20ms and 100ms for phase 1 and 2 respectively. At

the end of the discharge the plasma current is not zero. To null it, cooling down the plasma by allowing air to enter the VV breaking the vacuum would be a method to null out the plasma current. Regarding the eddy currents, they follow the expected behaviour according to the input currents. The highest values are about 30kA, which is about the plasma current in phase 1. The eddy currents at t=0ms are 1.6kA for phase 1 and 2.5kA for phase 2. Figure 6.5 includes the plasma current and its gradient, showing that the growth rates are kept within the desired range, from 1 to 10MA/s (1kA/ms=1MA/s).

6.2 Break-down results

6.2.1 Magnetic fields

The magnetic field at the start of the Sol ramp down (dot 3 in figure 6.3 (b) corresponding to t=0ms) have been calculated using the Grad-Shafranov solver. This calculation includes the eddy currents but not the plasma current, not started yet a this time. The Earth's field was also added to avoid extremely low values of the poloidal magnetic field, as commented on chapter 5.

Figure 6.6 includes plots of the toroidal field B_φ, the poloidal field B_θ and the LLoyd's critera, $E_\varphi B_\varphi / B_\theta$. Due to the symmetry of the field with respect to the Z=0 plane, only the upper portion of the VV is showed[1]. Small gaps are appreciable in the VV corners due to rounding issues, without further influence in the simulations. B_φ is the field created by the toroidal field coils, which decays with the radial position as $1/R$. The B_θ plots displays a more complicated pattern due to the addition of the eddy currents. Without the eddy currents, the lowest B_θ is contained within the polidal field null region (dashed in green), but the addition of the eddys create a more complicated pattern. This is a result of the fact that RZIp can not run using a target equilibrium which contains eddy currents, resulting in that the currents for the poloidal field null configuration (null currents) do not take into account the effect of the eddy currents. Hence, the eddy currents have to be added manually, worsening the field to the point that the lowest poloidal field is not in the poloidal field null region. In the central region of the VV, B_θ is about $1.1 \cdot 10^{-4}$T in phase 1 and $2.1 \cdot 10^{-4}$T in phase 2.

Regarding Lloyd's empirical criteria, it can be seen that the criteria for ohmic break-down is satisfied ($E_\varphi B_\varphi / B_\theta > 1000$V/m) near the inner wall in both phases, with a larger region in

[1] Actually, due to the addition of the Earth's field, the field is not completely symmetric with respect to the Z=0 plane, but the differences are negligible, about 10^{-7}T.

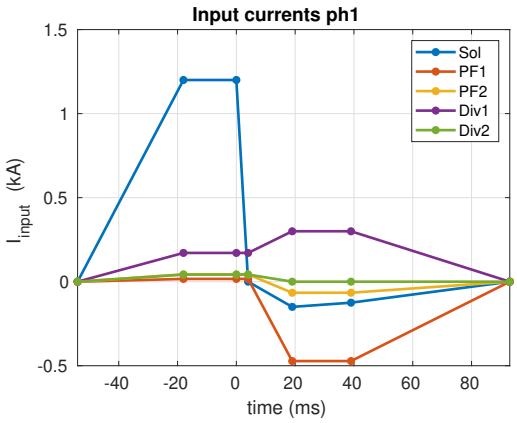

(a) Input currents of phase 1.

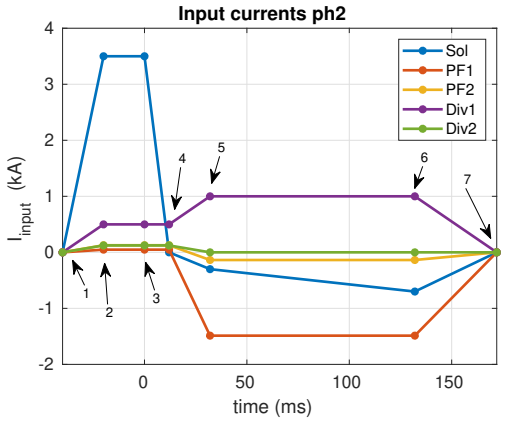

(b) Input currents of phase 2, indicating the discrete points of each of the waveforms.

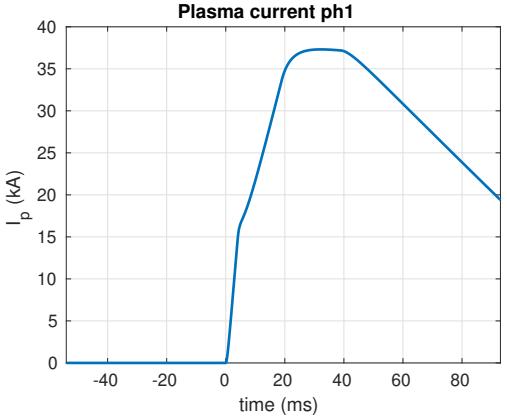

(c) Plasma current of phase 1.

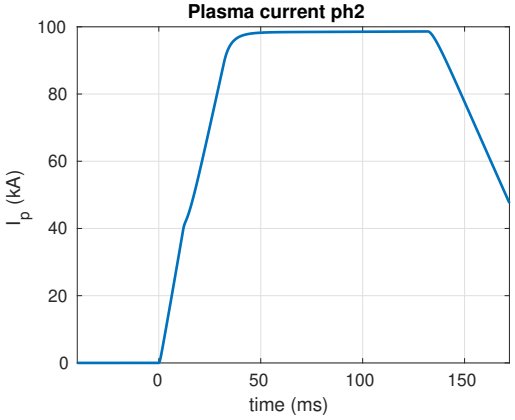

(d) Plasma current of phase 2.

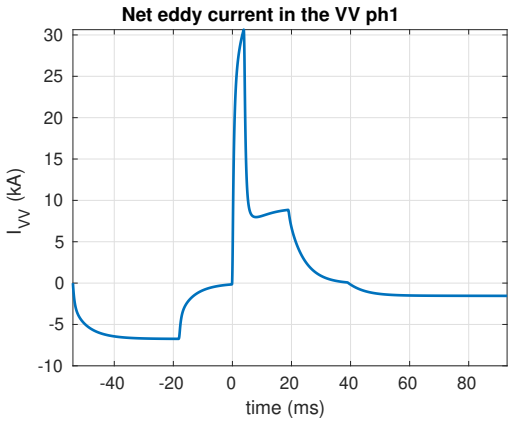

(e) Net eddy current in the VV of phase 1.

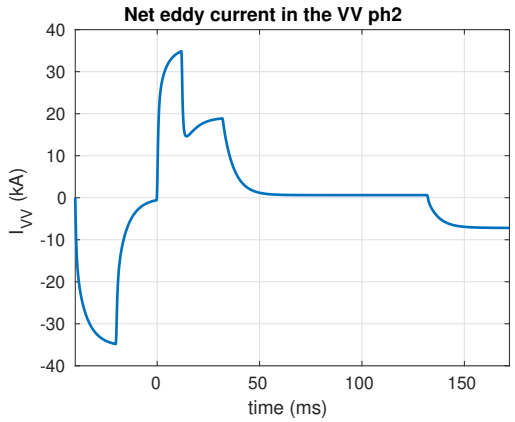

(f) Net eddy current in the VV of phase 2.

Figure 6.4. Coiset currents given as inputs and RZIp outputs for both phases, plasma current and the net eddy current induced in the vacuum vessel. The desired plasma current is sustained for 20ms in phase 1 and for 100ms in phase 2 (flat-top time).

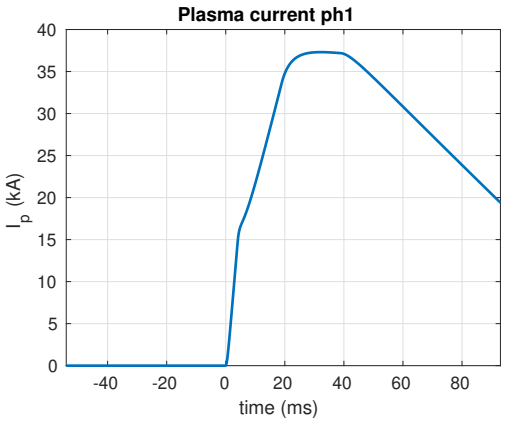

(a) Plasma current of phase 1.

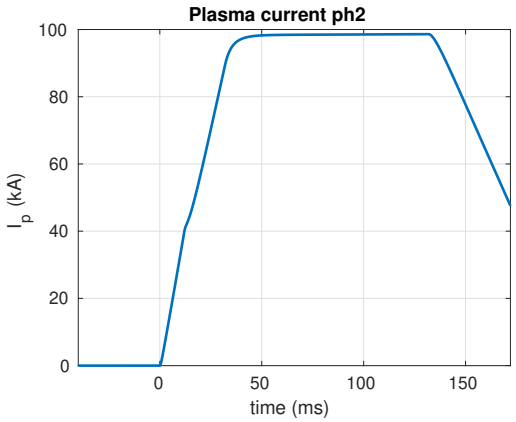

(b) Plasma current of phase 2, indicating the discrete points of each of the waveforms.

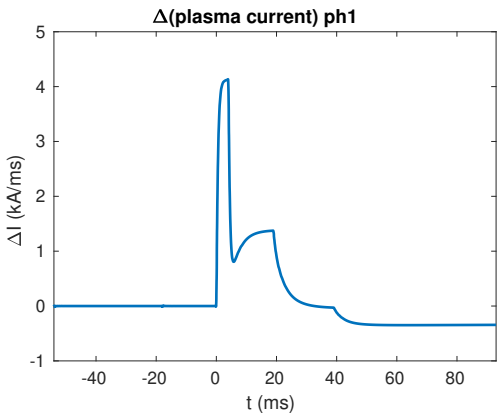

(c) Plasma current gradient of phase 1.

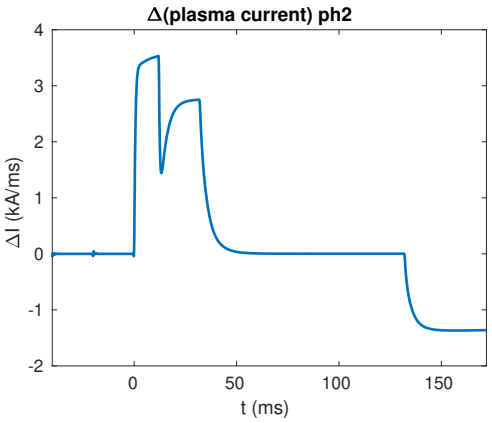

(d) Plasma current gradient of phase 2.

Figure 6.5. Plasma current and plasma current gradient for both phases.

phase 2 since this phase has larger B_φ.

6.2.2 Connection length

In this section, the connection length computed using both field line tracing and the empirical formula will be showed, as well as the potential gained by the electrons along their path.

Figure 6.7 shows the connection length obtained by field line tracing, the electric potential gained by the electrons and the grid used for the integration. The grid contains a meshgrid of 20x20 points, and the points located where the coils are have been removed. The resolution of the grid is 0.034m in the R axis and 0.0842 in the Z axis, giving a resolution relative to the VV size of 5.26% in both axis.

The first thing to note considering the connection length L plot is that it is not symmetric with respect to the $Z = 0$ plane . This is a consequence of the poloidal field, its components, B_R and B_Z. Figure 6.8 shows the vertical and radial field a t=0ms for phase 1 (it displays the

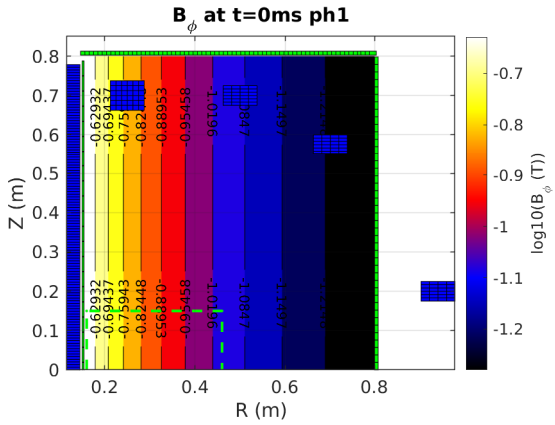

(a) Toroidal field of phase 1. $B_T(R_{\text{Geo}}) = 0.1\text{T}$.

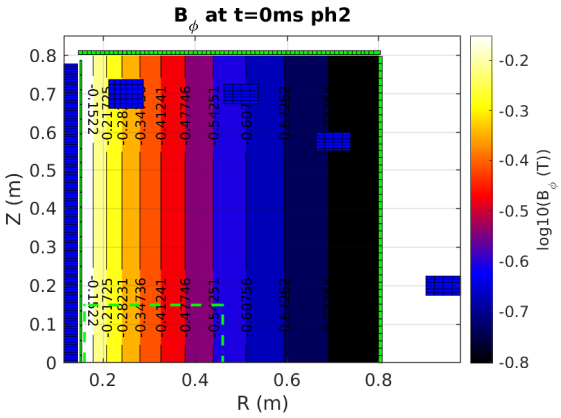

(b) Toroidal field of phase 2. $B_T(R_{\text{Geo}}) = 0.3\text{T}$.

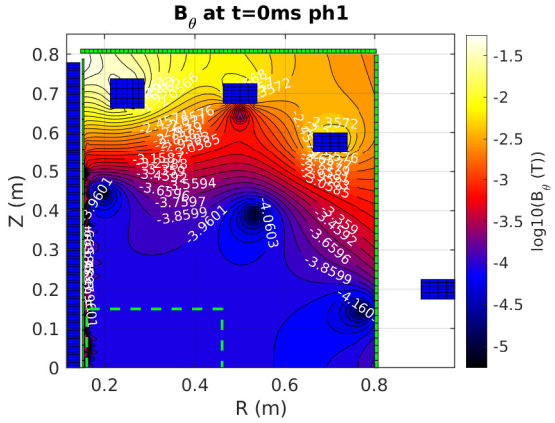

(c) Poloidal field of phase 1. $I_{\text{VV}}(t = 0) = 1.6\text{kA}$.

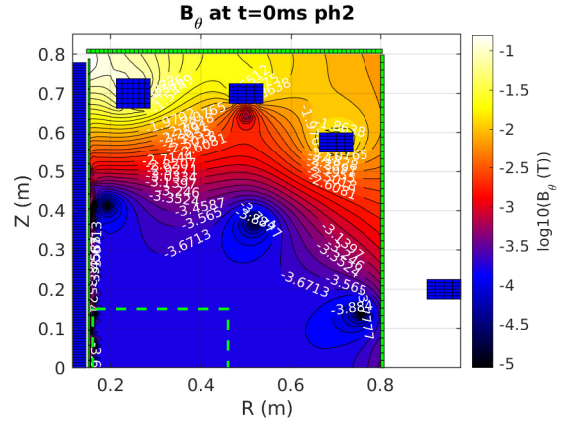

(d) Poloidal field of phase 2. $I_{\text{VV}}(t = 0) = 2.5\text{kA}$.

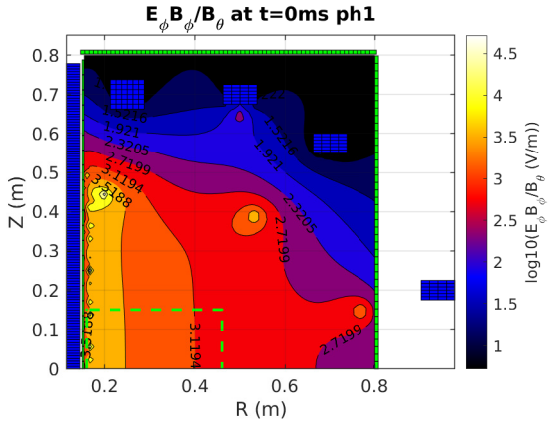

(e) Lloyd's criteria of phase 1.

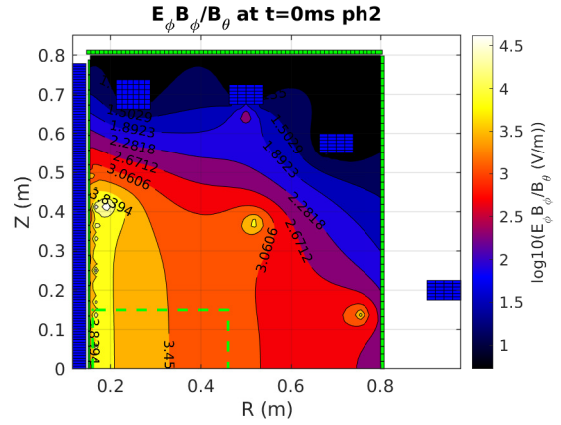

(f) Lloyd's criteria of phase 2.

Figure 6.6. Magnetic fields and Lloyd's criteria at t=0ms. Due to the symmetry with respect to Z=0, only the upper portion is shown. The poloidal field null region is dashed in green. Note in this plot the small gaps on the VV due to rounding issues can be seen.

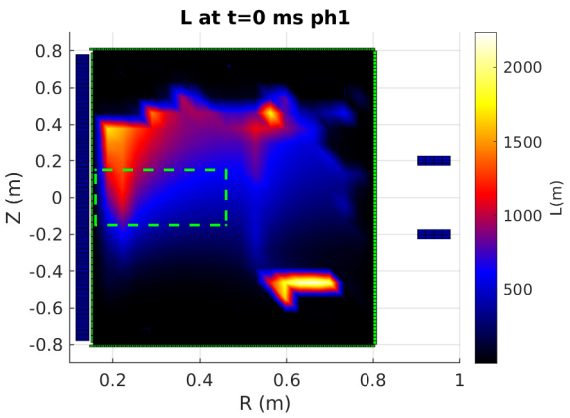

(a) Connection length of phase 1.

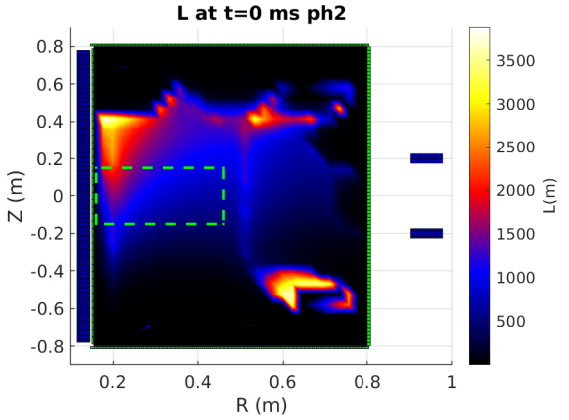

(b) Connection length of phase 2.

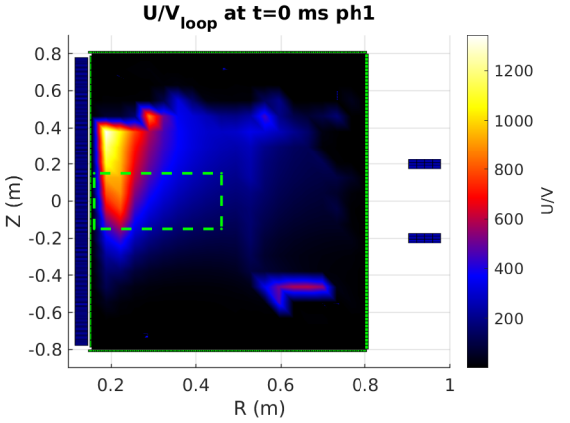

(c) U/V_{loop} of phase 1.

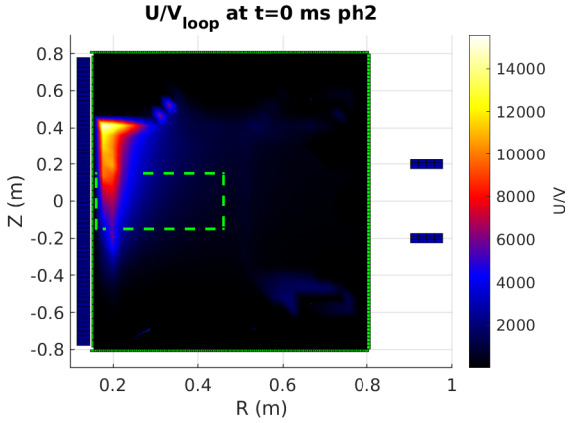

(d) U/V_{loop} of phase 2.

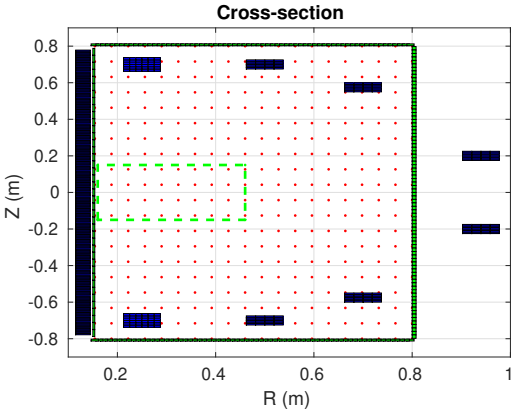

(e) Grid for the line tracing. It is a 20x20 grid, and the points where the coils are located in have been removed.

Figure 6.7. Connection length by line tracing and electric potential for SMART at t=0ms. The computational grid is also shown. The poloidal field null region is dashed in green. Note the connection length plot displays a region near the lower PF2 coil with high values, the lines wind up around the PF2 coil without colliding with it. This region do not appears in the electric potential plot confirming it is not relevant for the break-down.

same behaviour for phase 2). The Sol coil produces negative vertical field in the VV, and the PF and Div coils try to compensate it by creating positive vertical field. The resultant vertical field is mostly negative in the whole VV, but its magnitude has reduced. This explain the fact that the L plot is not symmetric, because the lines starting in the upper portion of the VV have on average higher connection length. Hence, the highest values of L are located at the upper portion of the VV. Higher values are obtained near the inner wall since there the toroidal field has its greatest values ($B_\varphi \propto 1/R$), making B_θ less relevant, resulting in lines that mostly goes in the toroidal direction, with little deviation.

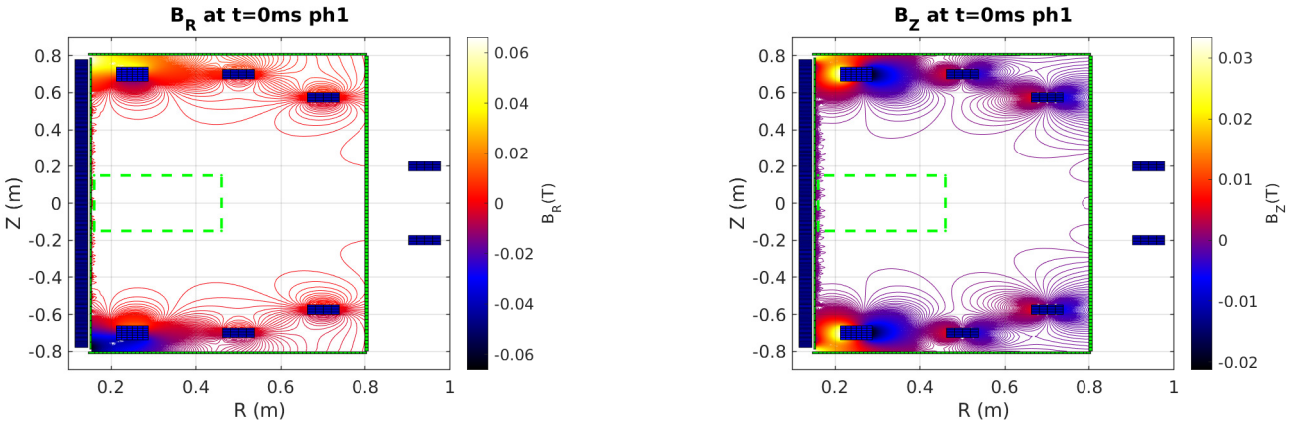

(a) Radial field.

(b) Vertical field.

Figure 6.8. Radial and vertical magnetic fields at t=0ms. The vertical component of the Sol field is negative, and the PF and Div coils try to null it by creating positive vertical field. The resultant vertical is mostly negative in the whole VV, but its magnitude has been reduced. The radial field is anti-symmetric and the vertical field symmetric with respect to the $Z = 0$ plane.

Nevertheless, the highest values appear in the surroundings of the lower PF2 coil ($Z = -0.6$m), because of the inhomogeneity of the field at the surroundings of a coil. Further from the coils, the field is more homogeneous, but at the surroundings on a coil, the field is mostly the field of the coil. Plots of several field lines are shown on figure 6.9, showing that some lines in the surroundings of the lower PF2 coil wind around them without colliding with them (the magnetic lines are twisted around the lower PF2 coil in a similar way the magnetic lines are twisted in a tokamak plasma). This figure also shows that, although the upper portion of the VV in general have higher connection lengths due to the fact that the vertical field is negative, if the lines start too high, they end up colliding rapidly with the upper coils or the upper VV wall.

Considering the U/V_{loop} plot, we see that the weird region surrounding the lower PF2 coil has low value of U/V_{loop} in comparison to the value of the upper portion of the VV near the

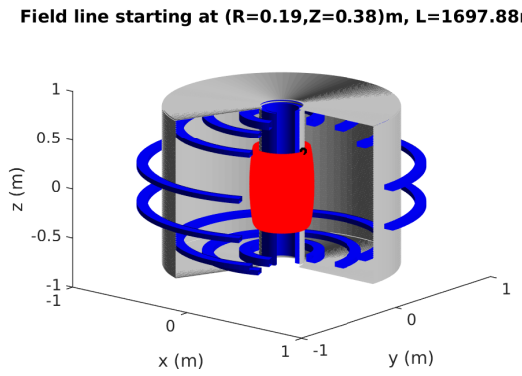

(a) Line starting in the upper portion of the VV with high L.

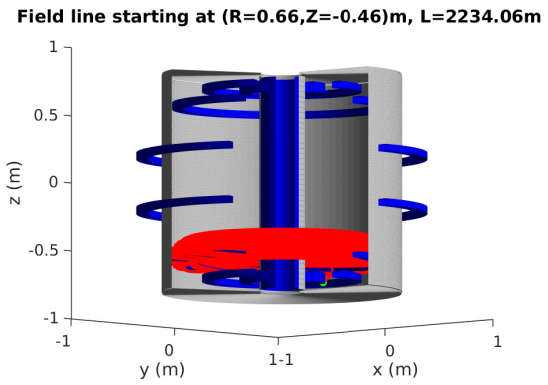

(b) Line starting on the surroundings of the lower PF2 coil.

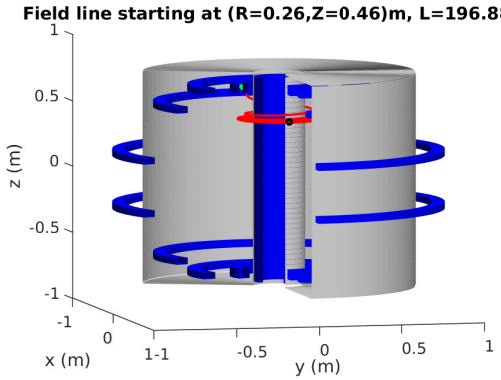

(c) Line starting on the upper portion of the VV with low L.

Figure 6.9. Magnetic field lines starting in the upper portion of the VV with high L (a), on the surroundings of the lower PF2 coil (b), and in the upper portion with low L (c). The starting point is denoted with a black dot, and the ending point with a green dot.

inner side, confirming this region is not important regarding break-down. As explained on section 3.1, this plot is more valuable than the B_θ or L plot since it also takes into account the energy gained by the electrons along their path. It can be seen that it displays roughly the same patter of the L plot, but removing this region around the lower PF2 and some regions with high L which are further from the inner VV wall.

Finally, the connection length in the poloidal field null region using the empirical formula will also be obtained, since it usually gives lower values than the connection length by field line tracing, which gives very high results. In spherical tokamaks (ST), L goes from 10 to 50m [26, 41]. The results obtained are cast in table 6.3. The value for the line tracing has been computed averaging the connection length values in the whole poloidal field null region. For the empirical formula, the two visions of a_{eff} have been used, being 0.15m for the ii) and 0.31m for the i), so the i) value will double the ii) value. The line tracing method gives about an order

of magnitude greater values than the ii) method. Phase 2 displays greater values than phase 1 because of the higher B_φ, that makes B_θ less relevant.

Phase	L(m)		
	Line tracing	Empirical ii)	Empirical i)
1	657.7	42.4	87.56
2	987.8	68.3	141.2

Table 6.3. Connection length at the poloidal field null region, computed via the empirical formula (3.5) and averaging the field line tracing method over the field null region surface. For the empirical formula, a_{eff} is 0.15m for the ii) version and 0.31m for the i) version.

6.2.3 Paschen curve and avalanche time

This section will review the Paschen curve's criteria and the estimation of the avalanche time.

The Paschen equation is (see 3.1)

$$E_{\varphi_{min}} = \frac{C_2 p}{\ln(C_1 p L)}, \tag{6.1}$$

and, given the connection length L and the pre-fill pressure p, it gives the minimum electric field needed to sustain the electron density. Since the connection length depends on both R and Z, the minimum electric field required will also depend on both R and Z. However, $E_{\varphi_{min}}(R, Z)$ as a function of p would need a 4D plot, so, instead, to create the Paschen's curve, an average value of L is chosen. This value is usually the value obtained by using the empirical formula, which is L at the poloidal field null region. Since this formula gives lower values than the values obtained by line tracing, this formula will be used here too. Regarding the electric field, it is given by $E = V_{\text{loop}}/2\pi R$ (see (3.21)), so the R coordinate needs to be chosen to do the Paschen's curve. It is often used R_{Geo}, which also serves as a guideline to compare with other reactors. However, due to the fact that the gas will break-down near the inner side, the coordinate $R_{\text{Geo}} - a \equiv R_{\text{in}}$, which is the inner R coordinate of the Last Closed Flux Surface (LCFS) for $Z = 0$ has also been used. For both phases, $R_{\text{Geo}} = 0.42$m and $R_{\text{Geo}} - a \equiv R_{\text{in}} = 0.19$m.

Figure 6.10 shows the Paschen's curve for SMART using both R_{Geo} and R_{in} for several L values between the range of the values obtained. The values of similar size tokamaks VEST and GlobusM are also dashed in the figure, whose values are also included in table 6.4. SMART values are included in table 6.5. For both phases, using $E(R_{\text{in}})$ break-down could be possible for $L \geq 30$m, while using $E(R_{\text{Geo}})$ $L \geq 70$m would be needed. SMART $E(R_{\text{Geo}})$ value is similar

	VEST	GlobusM
$p(10^{-5}\text{Torr})$	$2-3$	$3-6$
$V_{\text{loop}}(\text{V})$	3	4.5-8
$E(\text{V/m})$	1.2	1.8-3.1

Table 6.4. GlobusM [41] and VEST [26] break-down data. Both use H_2 as pre-fill gas. $E \equiv E(R_{\text{Geo}})$, where R_{Geo}=0.36m for GlobusM and 0.4m for VEST. VEST data correspond to break-down assisted with ECRH. GlobusM data is for ohmic solenoid. With ECRH, GlobusM needs 1-2V of V_{loop}.

to VEST value, but VEST uses ECRH assistance to get break-down. Ohmic break-down in GlobusM needs between 4.5 and 8V of V_{loop}, which is 1.5 and 2.7 times higher than SMART V_{loop}. However, it can be seen that $E(R_{\text{in}})$ is between GlobusM $E(R_{\text{Geo}})$ values. Using $E(R_{\text{Geo}})$ instead of $E(R_{\text{in}})$ gives additional safety, since if break-down is achieved at R_{Geo}, it will also be achieved on R_{in} ($B_\varphi \propto 1/R$).

Phase	$V_{\text{loop}}(\text{V})$	$E(R_{\text{in}})(\text{V/m})$	$E(R_{\text{geo}})(\text{V/m})$
1	2.98	2.49	1.06
2	2.90	2.39	1.03

Table 6.5. SMART loop voltage and electric field created by the Sol for both phases, using H_2 as pre-fill gas.

Nevertheless, as explained on section 3.1, Paschen's curve gives the electric field needed to sustain the electron density, so further information about whether break-down could be achieved or not is the calculation of the avalanche time, since the existence of the avalanche time implies the avalanche succeed.

Using (3.13) the avalanche time has been calculated as a function of p and E_φ for given L values, creating a plot similar to the Paschen's curve. For the pre-fill temperature, it has been used $T_{\text{pre}} = 20^{\text{o}}\text{C}$. For the L values, multiples of the empirical values obtained have been used (see table 6.3).

Figure 6.11 and 6.12 shows the avalanche time for several L for phase 1 and 2 respectively. Due to the lower connection length of phase 1, this phase will also need more time to end the break-down phase. The loop voltage of the Sol is induced for 4ms in phase 1 and 12ms in phase 2 (from do 3 to 4 in figure 6.4 (a) and (b), there are 4ms in phase 1, and 12ms in phase 2). Regarding the more conservatives value, the *ii*) method, $L_{\text{emp}}|_{ii)}$, about 4ms will be the minimum time for $p = 1.3 \cdot 10^{-4}\text{Torr}$, which is just the time the loop voltage is sustained in the Sol waveform on phase 1. Phase 2 would need 2.2ms with $p = 9.3 \cdot 10^{-5}\text{Torr}$, which a sixth of

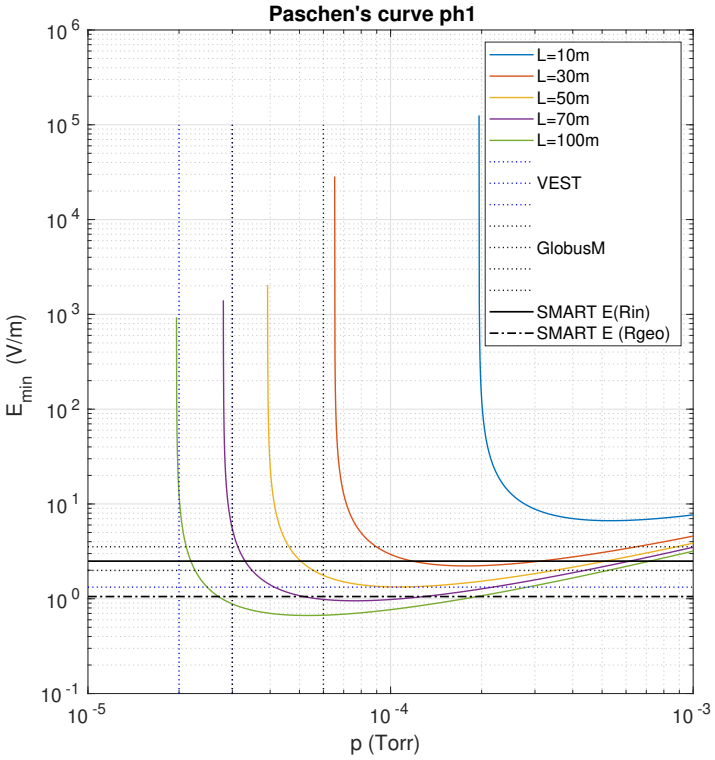

(a) Phase 1.

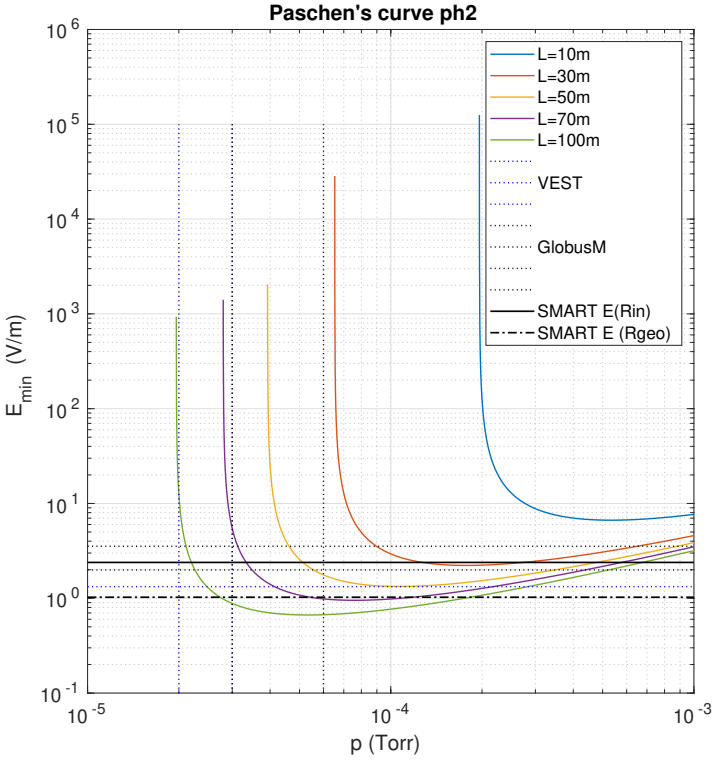

(b) Phase 2.

Figure 6.10. Paschen curves for SMART, showing VEST and GlobusM data. Hydrogen is used as the pre-fill gas in the three reactors.

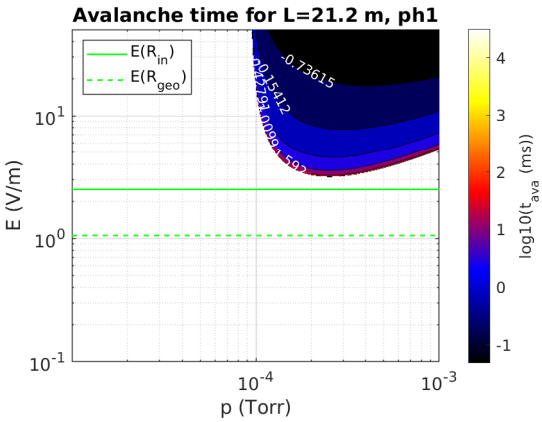

(a) $L = L_{\text{emp}}|_{ii)}/2$. No ohmic avalanche possible.

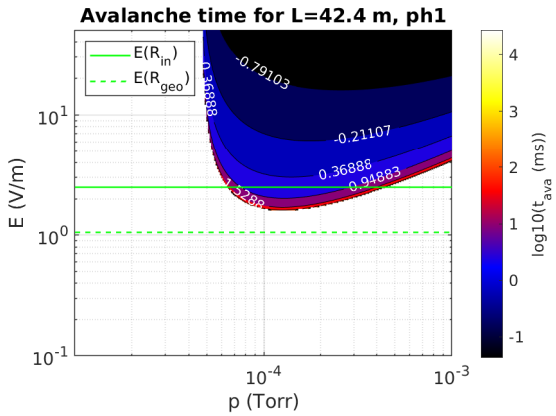

(b) $L = L_{\text{emp}}|_{ii)}$. Ohmic break-down possible using R_{in}. The minimum time is 3.9ms, for $p = 1.3 \cdot 10^{-4}$Torr.

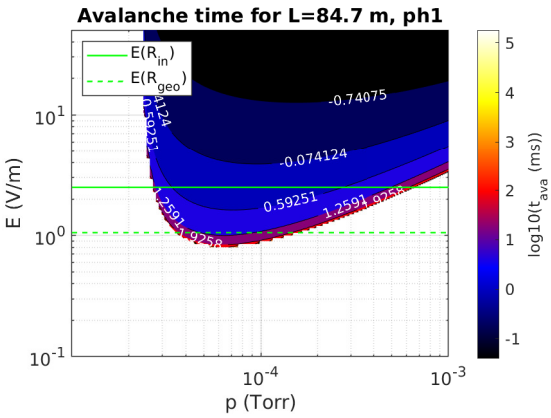

(c) $L = 2L_{\text{emp}}|_{ii)} \simeq L_{\text{emp}}|_{i)}$. Ohmic break-down possible using R_{in}. The minimum time is 1.7ms, for $p = 8.1 \cdot 10^{-5}$Torr.

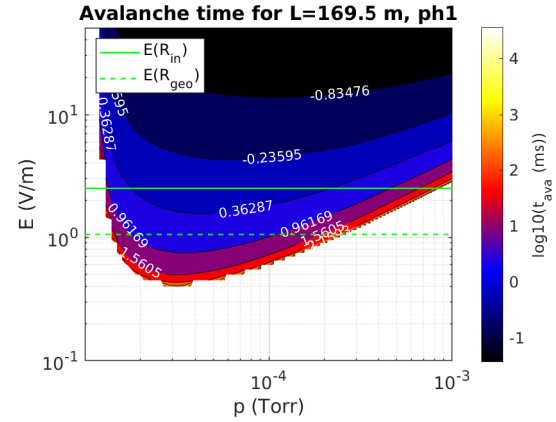

(d) $L = 4L_{\text{emp}}|_{ii)} \simeq 2L_{\text{emp}}|_{i)}$. Ohmic break-down possible using R_{in}. The minimum time is 1.2ms, for $p = 5.3 \cdot 10^{-4}$Torr.

Figure 6.11. Avalanche time for SMART phase 1, for multiples of the empirical connection length.

the time the loop voltage is sustained, 12ms. With the i) method, phase 1 would need 1.7ms, which is roughly half the time the loop voltage is sustained, and phase 2 would need 1.4ms, a similar time to what Tokamak Energy needs.

Figure 6.11 and 6.12 also contains the plots for half $L_{\text{emp}}|_{ii)}$, the worst scenario, and $4L_{\text{emp}}|_{ii)}$, the ideal scenario. In the worst scenario, no break-down would be possible in phase 1, although on figure 6.10, SMART E(R_{in}) tightly surpass the $L = 30$m. This remind us Paschen's curve not ensure avalanche, and that is why [25] recommends to double the minimum electric field to ensure break-down. For phase 2 it could be possible, but spending about 9.3ms in the optimal case. On the contrary, in the ideal case, $4L_{\text{emp}}|_{i)}$, both phases would need about 1ms in the optimal case, but the connection length may be too high.

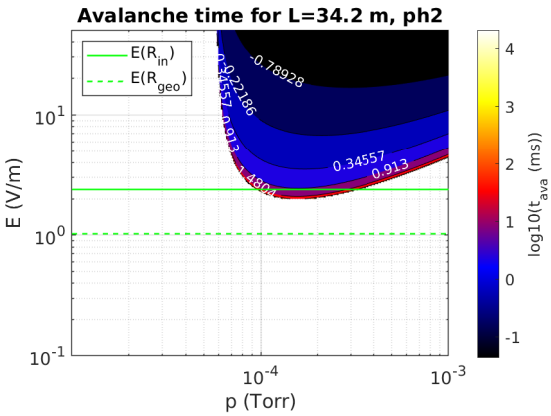

(a) $L = L_{\text{emp}}|_{ii)}/2$. Ohmic break-down possible using R_{in}. The minimum time is 9.3ms, for $p = 1.6 \cdot 10^{-4}$Torr

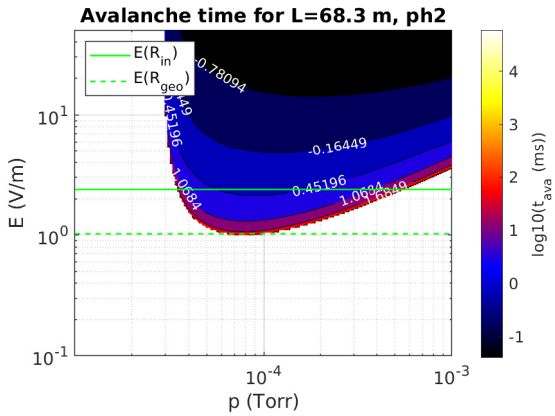

(b) $L = L_{\text{emp}}|_{ii)}$. Ohmic break-down possible using R_{in}. The minimum time is 2.2ms, for $p = 9.3 \cdot 10^{-5}$Torr.

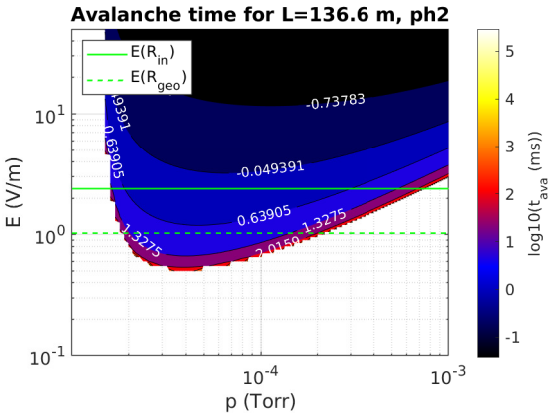

(c) $L = 2L_{\text{emp}}|_{ii)} \simeq L_{\text{emp}}|_{i)}$. Ohmic break-down possible using R_{in}. The minimum time is 1.4ms, for $p = 6.0 \cdot 10^{-5}$Torr.

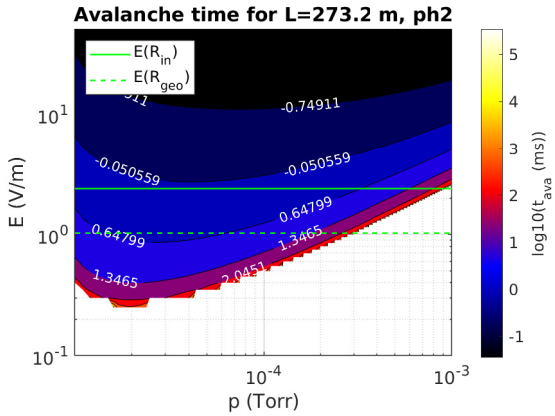

(d) $L = 4L_{\text{emp}}|_{ii)} \simeq 2L_{\text{emp}}|_{i)}$. Ohmic break-down possible using R_{in}. The minimum time is 1.0ms, for $p = 3.9 \cdot 10^{-5}$Torr.

Figure 6.12. Avalanche time for SMART phase 2, for multiples of the empirical connection length.

6.3 Discussion

In this section, the results obtained will be compared to other tokamaks of similar characteristics.

The first thing to compare is the poloidal field B_θ and Lloyd's criteria. Figure 6.13 shows a comparison between VEST B_θ and Lloyd's criteria with SMART phase 1, since for phase 1 the toroidal field B_φ is the same in both, 0.1T. The electric field is also very similar, 1.12 vs 1.06V/m. VEST achieves about 10^{-3}T in its central region, while we achieved 10^{-4}T. Roughly the same difference in values are found in VEST Lloyd's criteria plot. The figure also included a comparison with GlobusM poloidal field, comparing it with phase 2 because GlobusM has $B_T < 0.62$T. The minimum B_θ of GlobusM is 3.78G in the null region, while we achieve 2.13G

($10^{-3.6713}$T) in the null region, which is very similar to GlobusM value. However, although the agreement between our values and VEST and GlobuM values seems good enough, there is a source of imprecision in our simulations, and is the fact that RZIp do not run in a self-consistent manner with the eddy currents, as commented on section 6.2.1, so the null currents do not take into account the eddy currents, and the addition of the eddy currents worsen the field, so that the lowest poloidal field is not in the field null region. Another source of error is that our simulations use the ideal current waveforms, while more realistic simulations, such as VEST simulations, also simulate the power supplys of the coils. As a conclusion for this magnetic field comparison, other effects such as errors in the coil windings or magnetic material materials surrounding the VV could also alter the magnetic field.

Considering now the connection length L by line tracing, figure 6.14 include a comparison with NSTX and phase 2, because NSTX has $B_\varphi = 0.3$T [42]. The values of both phase 2 and NSTX are about km long, but the appearance of both plots are not very similar. This difference is caused by the fact that SMART has most of its coils inside the VV, while NSTX has its coils outside, as can be seen on (d). To prove this point, a L plot of an older SMART configuration with all the coils outside (phase 1) is included (c), showing similarities with the NSTX plot; both plots displays high L arm-like regions, pointing upward and outward (to the outer wall). However, SMART do not have an arm pointing downward while NSTX do, and this arm seems to be caused by a lower PF coil of NSTX, PF1B, which do not appears in the upper portion of the NSTX cross-section (i.e., NSTX cross-section do not displays symmetry with respect to the $Z = 0$ plane). The connection length computed by the empirical formula is roughly an order of magnitude lower than the connection length obtained by field line tracing. Differences larger than a factor of two were predicted in [23] and differences about an order of magnitude, as obtained in this work, were obtained in ITER simulations [25].

Regarding Paschen's curve and avalanche time, SMART loop voltage seem a bit low in comparison to GlobusM, but since the loop voltage is strongly dependent on the configuration of the machine, which is different for each machine, is not such a determinant factor. Instead, studying other variables such as the avalanche time would give more information, and in our case the avalanche time confirm that the break-down phase could be finished in a short enough time interval, going from 1 to 4ms for pre-fill pressures about 10^{-4}Torr. Data reconstruction in a VEST discharge using ECRH assistance shows that the plasma has already formed and moved to the outer wall 2ms after the ramp-down of the Sol, so the avalanche time must be $\leq$ 2ms [26]. This time interval lies between the range of values obtained for SMART, with the difference that the SMART results have been obtained with an ohmic startup, without any

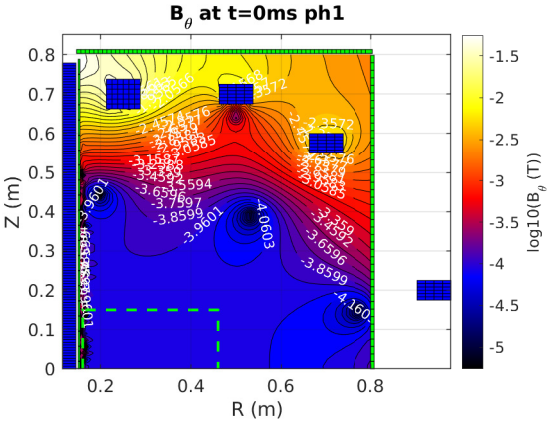

(a) Poloidal field of SMART phase 1.

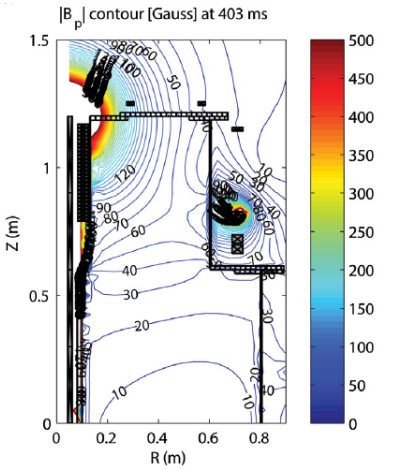

(b) Poloidal field of VEST. $1G = 10^{-4}$T.

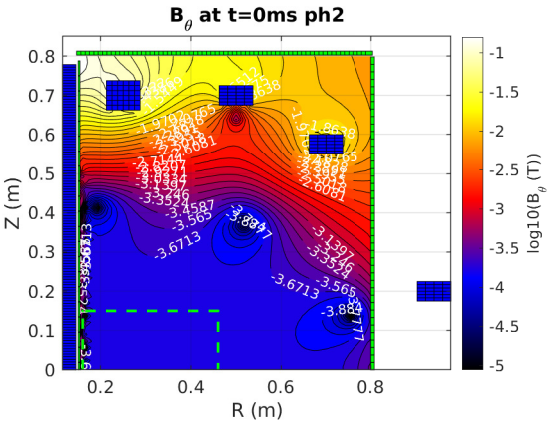

(c) Poloidal field of SMART phase 2.

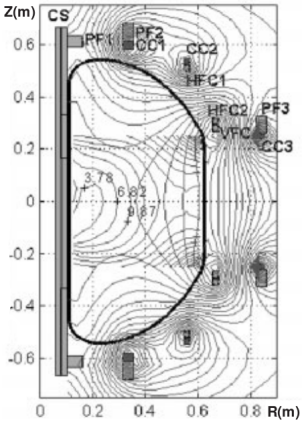

(d) Poloidal field of GlobusM.

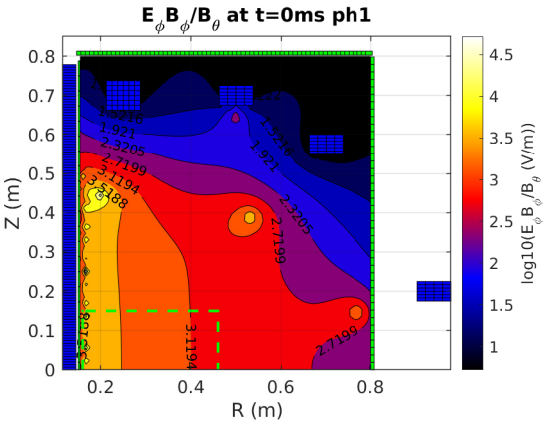

(e) Lloyd's criteria of SMART phase 1.

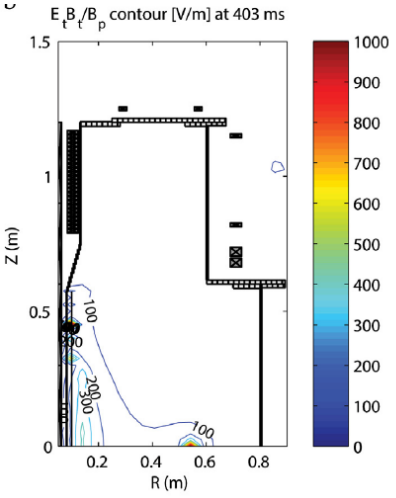

(f) Lloyd's criteria of VEST.

Figure 6.13. Comparison of the poloidal field and Lloyd's criteria with VEST [26] and GlobusM [41] (both simulated data) at the exact time when the loop voltage is induced. Phase 1 is used to compare with VEST because it the same $B_\varphi = 0.1$T. $E_\varphi = 1.12$V/m for VEST and 1.06V/m for phase 1. $B_\varphi < 0.62$T for GlobusM, so it is compared with phase 2, which has 0.3T.

assistance. However, SMART will also have ECRH assistance for the break-down just in case it is needed to ionize the pre-fill gas.

Nevertheless, the loop voltage calculated here is the loop voltage induced by only the Sol, excluding the effect of the eddy currents, which will decrease the loop voltage according to Lenz's law. A more precise simulation should compute the loop voltage in a self-consistent manner with the eddy currents.

Finally, the simulations carried out here, and in most of the bibliography regarding break-down studies, are done ignoring the time dependence of all the variables such as the connection length or the poloidal field, so they have to be treated as a first approximation to the problem of the tokamak start-up (to deduce (3.7), the time dependence of the loss rate was neglected). Also, the plasma current needs to be considered since shortly after the loop voltage is induced, the plasma current will be high enough to create non-negligible field as compared to the structure's field. For deeper studies of the start-up phase, specific codes have been developed to simulate all the stages of the start-up phase such as DYON [21] or DINA, which consider the time dependence of the loss rate and the role of the plasma current in the magnetic fields.

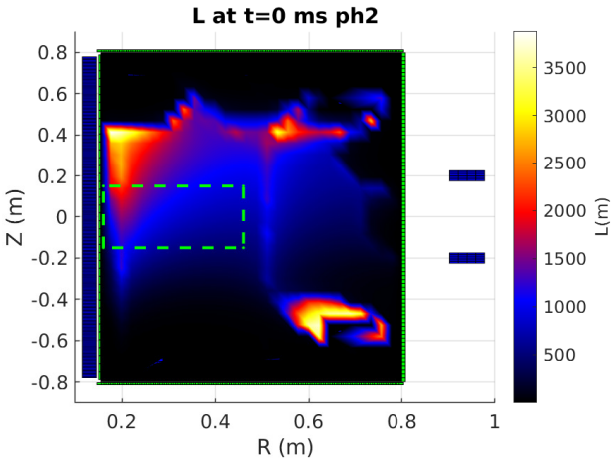

(a) Connection length of SMART phase 2.

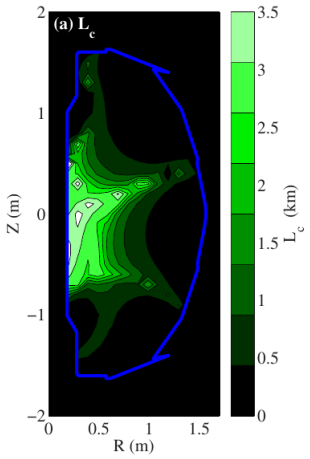

(b) Connection length of NSTX.

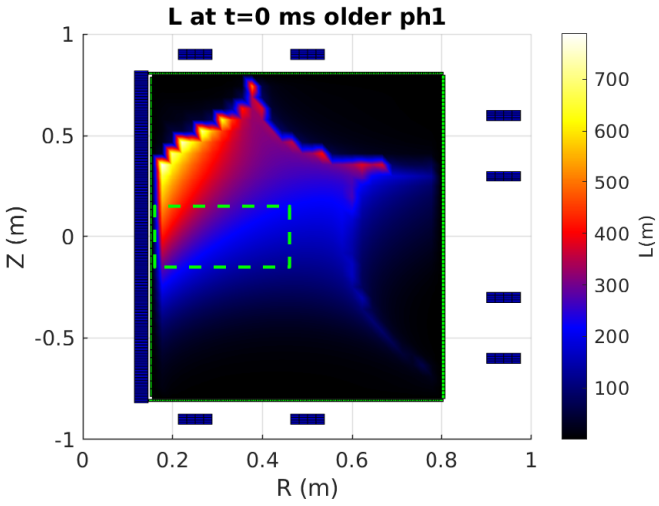

(c) Connection length of an older SMART phase 1 with the coils outside (S1-014).

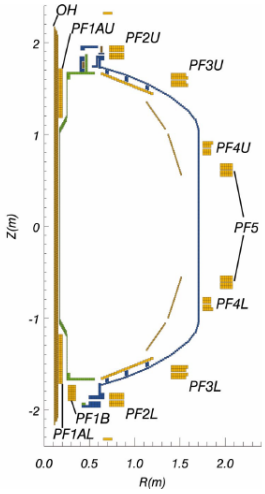

(d) Cross-section of NSTX.

Figure 6.14. Comparison of the connection length plot with NSTX [28, 43] (simulated data). $B_\varphi = 0.3$T for NSTX and for phase 2.

Chapter 7

Summary and conclusions

The break-down phase of the future SMART reactor of the University of Seville has been modelled numerically using the Fiesta toolbox. The fundamentals of tokamak physics and tokamak start-up have been reviewed to understand the foundation of this work.

The work of this thesis summarizes months of working in the design of the SMART reactor along with the SMART team of the PSFT group, composed of physicists and engineers students and researchers, showing the most updated scenarios for the initial operational phase of SMART and a future upgrade.

The coil currents have been optimized to achieve the same target equilibrium on both phases and to ensure the break-down of the pre-fill gas, hydrogen, without any assistance method. For pre-fill pressures about 10^{-4}Torr, the gas will last between 2 and 4 ms to break-down. The eddy currents have been included in the calculations, since they play an important role in the break-down phase altering the poloidal magnetic field inside the vacuum vessel (VV). Poloidal field values around 1.1 and $2.1 \cdot 10^{-4}$T are obtained in the poloidal field null region.

The connection length has been computed by field line tracing and by using an empirical formula, giving the first method about an order of magnitude greater values than the second one. The electric potential gained by an electron following the field lines has also been calculated to estimate where the gas will break-down and turns into a plasma. The gas will break-down in the upper portion of the VV, near the inner VV wall.

This work presents the first approach to study the break-down phase of the tokamak start-up. Further studies such as the use of specific codes to model the entire tokamak start-up phase are required to ensure proper plasma initiation. Also, a deeper understanding of the Fiesta toolbox is needed for self-consistent simulations. For more realistic simulations, the power supply's behaviour should be included in the simulations, as well as a more realistic VV.

Chapter 8

Bibliography

[1] G.R. Satchler. Introduction to nuclear reactions. Macmillan, 2008.

[2] Kenneth S. Krane. Introductory nuclear physics. John Wiley & sons, 2008.

[3] K. Miyamoto. Plasma physics for controlled fusion. Springer, 2004.

[4] J. Wesson. Tokamaks. Oxford University Press, Oxford, 2004.

[5] Francis F. Chen. Introduction to Plasma Physics and Controlled Fusion. Springer International Publishing, 2016.

[6] Roger A. Freedman Hugh D. Young. University Physics, with Modern Physics. Pearson, 2020.

[7] A. Pironti and M. Walker. Fusion, tokamaks, and plasma control: an introduction and tutorial. IEEE Control Systems Magazine, 25(5):30–43, 2005.

[8] A. Beghi and A. Cenedese. Advances in real-time plasma boundary reconstruction: from gaps to snakes. IEEE Control Systems Magazine, 25(5):44–64, 2005.

[9] M. Ariola and A. Pironti. Plasma shape control for the jet tokamak: an optimal output regulation approach. IEEE Control Systems Magazine, 25(5):65–75, 2005.

[10] G. Ambrosino and R. Albanese. Magnetic control of plasma current, position, and shape in tokamaks: a survey or modeling and control approaches. IEEE Control Systems Magazine, 25(5):76–92, 2005.

[11] Linjin Zheng. Advanced tokamak stability theory. Morgan & Claypool Publishers, 2015.

[12] Zhe Gao. Compact magnetic confinement fusion: Spherical torus and compact torus. Matter and Radiation at Extremes, 1(3):153 – 162, 2016.

[13] Y-K.M. Peng and D.J. Strickler. Features of spherical torus plasmas. Nuclear Fusion, 26(6):769–777, jun 1986.

[14] A. Mancini, J. Ayllon-Guerola, S. J. Doyle, M. Agredano-Torres, D. Lopez-Aires, J. Toledo-Garrido, C. Soria-Hoyo, E. Viezzer, M. Garcia-Munoz, PF. Buxton, K.-J. Chung, J. Garcia-Dominguez, MP. Gryaznevich, J. Hidalgo-Salaverri, Y.-S. Hwang, and J. Segado-Fernández. Mechanical and electromagnetic design of the vacuum vessel of the smart tokamak. In 31st Symposium on Fusion Technology (SOFT-31), 2020.

[15] Jefrrey P. Freidberg. Ideal magnetohydrodynamics. Plenum Press, 1987.

[16] T C Luce. An analytic functional form for characterization and generation of axisymmetric plasma boundaries. Plasma Physics and Controlled Fusion, 55(9):095009, jul 2013.

[17] Y.-K. M. Peng. The physics of spherical torus plasmas. Physics of Plasmas, 7(5):1681–1692, 2000.

[18] D. Mueller. The physics of tokamak start-up. Physics of Plasmas, 20(5):058101, 2013.

[19] P.C. de Vries and Y. Gribov. Iter breakdown and plasma initiation revisited. Nuclear Fusion, 59(9):096043, aug 2019.

[20] Joyeeta Sinha. Plasma breakdwon and current formation in single core and doublet configurations on TCV. PhD thesis, École Polytechnique Fédérale de Laussane, 2017.

[21] Hyun-Tae Kim. Physics and computational simulatios of plasma burn-through for tokamak start-up. PhD thesis, Imperial college of Science Technology and Medicine, London, 2013.

[22] B Lloyd, P G Carolan, and C D Warrick. Ecrh-assisted start-up in ITER. Plasma Physics and Controlled Fusion, 38(9):1627–1643, sep 1996.

[23] B. Lloyd, G.L. Jackson, T.S. Taylor, E.A. Lazarus, T.C. Luce, and R. Prater. Low voltage ohmic and electron cyclotron heating assisted startup in diii-d. Nuclear Fusion, 31(11):2031–2053, nov 1991.

[24] ITER Physics Expert Group on Disruptions, Plasma Control, ITER Physics Expert Group on Energetic Particles, Heating MHD, Current Drive, ITER Physics Expert Group on Di-

agnostics, and ITER Physics Basis Editors. Chapter 8: Plasma operation and control. Nuclear Fusion, 39(12):2577–2625, dec 1999.

[25] Y Gribov, D Humphreys, K Kajiwara, E.A Lazarus, J.B Lister, T Ozeki, A Portone, M Shimada, A.C.C Sips, and J.C Wesley. Chapter 8: Plasma operation and control. Nuclear Fusion, 47(6):S385–S403, jun 2007.

[26] YoungHwa An, Jeongwon Lee, HyunYeong Lee, JongGab Jo, Bong-Ki Jung, Kyoung-Jae Chung, Young-Gi Kim, Jungmin Jo, Jeong hun Yang, Yong-Su Na, T.S. Hahm, and Y.S. Hwang. Plasma start-up design and first plasma experiment in vest. Fusion Engineering and Design, 96-97:274 – 280, 2015. Proceedings of the 28th Symposium On Fusion Technology (SOFT-28).

[27] E.A Lazarus, A.W Hyatt, G.L Jackson, and D.A Humphreys. Using a multipole expansion for startup in the diii-d tokamak. Nuclear Fusion, 38(7):1083–1096, jul 1998.

[28] K.C. Hammond, R. Raman, and F.A. Volpe. Application of townsend avalanche theory to tokamak startup by coaxial helicity injection. Nuclear Fusion, 58(1):016013, nov 2017.

[29] David J. Griffiths. Introduction to electrodynamics. Prentice Hall, New Jersey, 1999.

[30] L. Pangione, G. McArdle, and J. Storrs. New magnetic real time shape control for mast. Fusion Engineering and Design, 88(6):1087 – 1090, 2013. Proceedings of the 27th Symposium On Fusion Technology (SOFT-27); Liège, Belgium, September 24-28, 2012.

[31] M J Windridge, G Cunningham, T C Hender, R Khayrutdinov, and V Lukash. Nonlinear instability at large vertical displacements in the mast tokamak. Plasma Physics and Controlled Fusion, 53(3):035018, feb 2011.

[32] L.L. Lao, H. St. John, R.D. Stambaugh, A.G. Kellman, and W. Pfeiffer. Reconstruction of current profile parameters and plasma shapes in tokamaks. Nuclear Fusion, 25(11):1611–1622, nov 1985.

[33] Alfredo Pironti Marco Ariola. Magnetic control of tokamak plasmas. Springer, 2008.

[34] Atul Stefan Sharma. Tokamak modelling and control. PhD thesis, Imperial college of Science Technology and Medicine, London, 2002.

[35] J.B. Lister, A. Sharma, D.J.N. Limebeer, Y. Nakamura, J.P. Wainwright, and R. Yoshino. Plasma equilibrium response modelling and validation on jt-60u. Nuclear Fusion, 42(6):708–724, jun 2002.

[36] S. J. Doyle, A. Mancini, M. Agredano-Torres, J. L. Garcia-Sanchez, J. M. Ayllon-Guerola, D. Lopez-Aires, M. Garcia-Munoz, E. Viezzer, C. Soria-Hoyo, P. F. Buxton, M. P. Gryaznevich, Y.-S. Hwang, and K.-J. Chung. Equilibrium design for the smart tokamak. In 31st Symposium on Fusion Technology (SOFT-31), 2020.

[37] Peter Buxton. Merging/compression start-up in st40: Analysis of first experimental results. In 45th EPS Conference on Plasma Physics, 07 2018.

[38] K.J. Chung, Y.H. An, B.K. Jung, H.Y. Lee, J.J. Dang, J.W. Lee, J. Yang, J.G. Jo, D.H. Choi, Y.G. Kim, Y.S. Na, and Y.S. Hwang. Initial plasma start-up using partial solenoid coils in versatile experiment spherical torus (vest). Fusion Engineering and Design, 88(6):787 – 790, 2013. Proceedings of the 27th Symposium On Fusion Technology (SOFT-27); Liège, Belgium, September 24-28, 2012.

[39] V Mertens, Guenter Haas, V. Rohde, and ASDEX Team. Hydrogen gas balance in asdex upgrade with div iib. In Koch, R.; Lebedev, S.: 30th EPS Conference on Plasma Physics and Controlled Fusion, European Physical Society (2003), 01 2003.

[40] X. Song, X.R. Duan, X.M. Song, G.Y. Zheng, S. Wang, B. Li, X.Y. Bai, Sh.D. Song, C. Wang, and J. Sun. Experimental results of plasma breakdown and flux optimization on hl-2a tokamak. Fusion Engineering and Design, 125:195 – 198, 2017.

[41] V.K Gusev, T.A Burtseva, A.V Dech, G.A Gavrilov, V.E Golant, S.V Krikunov, R.G Levin, V.B Minaev, A.B Mineev, O.A Minyaev, E.E Mukhin, A.N Novokhatskii, Yu.V Petrov, E.N Rumyantsev, N.V Sakharov, and V.M Sharapov. Plasma formation and first oh experiments in the globus-m tokamak. Nuclear Fusion, 41(7):919–925, jul 2001.

[42] Stanley M. Kaye, Masayuki Ono, Yueng-Kay Martin Peng, Donald B. Batchelor, Mark D. Carter, Wonho Choe, Robert Goldston, Yong-Seok Hwang, E. Fred Jaeger, Thomas R. Jarboe, Stephen Jardin, David Johnson, Robert Kaita, Charles Kessel, Henry Kugel, Rajesh Maingi, Richard Majeski, Janhardan Manickam, Jonathan Menard, David R. Mikkelsen, David J. Orvis, Brian A. Nelson, Franco Paoletti, Neil Pomphrey, Gregory Rewoldt, Steven Sabbagh, Dennis J. Strickler, Edmund Synakowski, and James R. Wilson. Physics design of the national spherical torus experiment. Fusion Technology, 36(1):16–37, 1999.

[43] D. A. Gates, J. E. Menard, and R. J. Marsala. Vessel eddy current measurement for the national spherical torus experiment. Review of Scientific Instruments, 75(12):5090–5093, 2004.

[44] Norman S. Nise. Control system engineering. Wiley, 2019.

Appendix A

Calculation of the voltage induced by a solenoid of finite width

The magnetic field $\vec{B}$ of a solenoid of inner radius R_{in} and outer radius $R_{\text{out}}(< R_{\text{in}})$, ignoring border effects (i.e., assuming infinite length), ca be easily calculated using Ampère's law, giving:

$$\vec{B}_{\text{Sol}} = \hat{Z} \begin{cases} \mu_0 I \dfrac{N}{l} & R < R_{\text{in}} \\ \mu_0 I \dfrac{N}{l}\left(1 - \dfrac{R - R_{\text{in}}}{R_{\text{out}} - R_{\text{in}}}\right) & R_{\text{in}} < R < R_{\text{out}} \\ 0 & R > R_{\text{out}} \end{cases} \tag{A.1}$$

where N is its number of turns and l the length of the Sol, and I the intensity of each turn, I_{Sol}[1].

The normal vector $\vec{n}$ on (3.14) is chosen to be $\hat{Z}$, so the loop voltage is

$$V_{\text{loop}} = -\frac{d}{dt}\int_S B_{\text{Sol}} dS = -\int_S \frac{dB_{\text{Sol}}}{dt} dS, \tag{A.2}$$

introducing the derivative into the integral since the integration variables do not vary, the only thing that vary is the Sol current. The derivate of the Sol current can be computed since the Sol current is decreased linearly, so it satisfies

$$I_{\text{Sol}}(t) = mt + n. \tag{A.3}$$

At $t = 0$, $I_{\text{Sol}} \equiv I_0$, and the ramp goes down until $I_{\text{Sol}}(t_1) \equiv I_1$ $(I_0 > I_1)$, so the Sol current is

$$I_{\text{Sol}}(t) = \frac{I_1 - I_0}{t_1} t + I_0. \tag{A.4}$$

[1]Note the boundary conditions of the magnetic field are satisfied, the field is continuous since there is no surface charge density at R_{in} or at R_{out}.

To solve (3.15), the integral has to be divided into the three intervals that $\vec{B}_{\text{Sol}}$ has:

$$\int_S \frac{dB_{\text{Sol}}}{dt} dS = \int_{0<R<R_{\text{in}}} \frac{dB_{\text{Sol}}}{dt} dS + \int_{R_{\text{in}}<R<R_{\text{out}}} \frac{dB_{\text{Sol}}}{dt} dS + \cancelto{0}{\int_{R_{\text{out}}<R} \frac{dB_{\text{Sol}}}{dt} dS}; \tag{A.5}$$

Let'solve each term separately:

- $\displaystyle\int_{0<R<R_{\text{in}}} \frac{dB_{\text{Sol}}}{dt} dS = \int_{0<R<R_{\text{in}}} \mu_0 \frac{dI}{dt} \frac{N}{l} dS = \mu_0 \frac{dI}{dt} \frac{N}{l} \pi R_{\text{in}}^2,$
- $\displaystyle\int_{R_{\text{in}}<R<R_{\text{out}}} \frac{dB_{\text{Sol}}}{dt} dS = \int_{0<R<R_{\text{in}}} \mu_0 \frac{dI}{dt} \frac{N}{l} \Big(1 - \frac{R - R_{\text{in}}}{R_{\text{out}} - R_{\text{in}}}\Big) dS = \mu_0 \frac{dI}{dt} \frac{N}{l} \Big[$

  $\displaystyle\int_{R_{\text{in}}}^{R_{\text{out}}} \int_0^{2\pi} R dR d\varphi - \frac{1}{R_{\text{out}} - R_{\text{in}}} \int_{R_{\text{in}}}^{R_{\text{out}}} \int_0^{2\pi} (R - R_{\text{in}}) R dR d\varphi \Big] = \mu_0 \frac{dI}{dt} \frac{N}{l} \Big[$

  $\displaystyle\pi(R_{\text{out}}^2 - R_{\text{in}}^2) - \frac{2\pi}{R_{\text{out}} - R_{\text{in}}} \Big(\frac{1}{3}(R_{\text{out}}^3 - R_{\text{in}}^3) - \frac{R_{\text{in}}}{2}(R_{\text{out}}^2 - R_{\text{in}}^2)\Big)\Big].$

The loop voltage induced is, taking into account (A.3),

$$V_{\text{loop}} = -\mu_0 \frac{N}{l} \frac{I_1 - I_0}{t} \Big[\pi R_{\text{in}}^2 + \pi(R_{\text{out}}^2 - R_{\text{in}}^2) - \frac{2\pi}{R_{\text{out}} - R_{\text{in}}} \Big(\frac{1}{3}(R_{\text{out}}^3 - R_{\text{in}}^3) - \frac{R_{\text{in}}}{2}(R_{\text{out}}^2 - R_{\text{in}}^2)\Big)\Big]. \tag{A.6}$$

With the normal vector choice, the loop voltage is positive.

Appendix B

State space representation

The state space representation is a mathematical model of a physical system, whose scheme is shown in figure B.1. The system can be represented by the following system of equations [44] (section 3.3)

$$\begin{cases} \dfrac{d\boldsymbol{x}}{dt} = \boldsymbol{A}\boldsymbol{x} + \boldsymbol{B}\boldsymbol{u}, \\ \boldsymbol{y} = \boldsymbol{C}\boldsymbol{x} + \boldsymbol{D}\boldsymbol{u}, \end{cases} \tag{B.1}$$

The column vector $\boldsymbol{x}$ contains the state space variables (the minimun set of variables needed to determine the system), and it is called the *state vector*. $\boldsymbol{u}$ is the *input or control vector*, which contains the input variables, and $\boldsymbol{y}$ is the *output vector*, and contains the output variables. $\boldsymbol{A}$ is the *system matrix*, and defines the first-order differential equations that determines the state variables, $\boldsymbol{B}$ is the *input matrix*, which relates the input variables with the time derivatives of the state variables. $\boldsymbol{C}$ is the *output matrix*, which defines the set of equations that determines the output variables as a combination of the state space variables and the inputs, and $\boldsymbol{D}$ is the *feedforward matrix*, which relates the input and output variables.

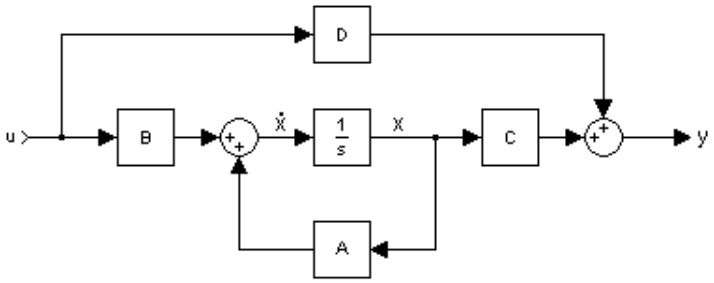

Figure B.1. Block diagram representation of the linear state-space equations.